HHS Public Access

Author manuscript

Cell Rep. Author manuscript; available in PMC 2023 October 23.

Published in final edited form as:

Cell Rep. 2023 June 27; 42(6): 112552. doi:10.1016/j.celrep.2023.112552.

The adhesion GPCRs CELSR1–3 and LPHN3 engage G proteins via distinct activation mechanisms

Duy Lan Huong Bui[1], **Andrew Roach**[1], **Jingxian Li**[2], **Sumit J. Bandekar**[2], **Elizabeth Orput**[1], **Ritika Raghavan**[1], **Demet Araç**[2], **Richard C. Sando**[1,3,*]

[1]Department of Pharmacology, Vanderbilt Brain Institute, Vanderbilt University, Nashville, TN 37240, USA

[2]Department of Biochemistry and Molecular Biology, The University of Chicago, Chicago, IL 60637, USA

[3]Lead contact

SUMMARY

Adhesion G protein-coupled receptors (aGPCRs) are a large GPCR class that direct diverse fundamental biological processes. One prominent mechanism for aGPCR agonism involves autoproteolytic cleavage, which generates an activating, membrane-proximal tethered agonist (TA). How universal this mechanism is for all aGPCRs is unclear. Here, we investigate G protein induction principles of aGPCRs using mammalian latrophilin 3 (LPHN3) and cadherin EGF LAG-repeat 7-transmembrane receptors 1–3 (CELSR1–3), members of two aGPCR families conserved from invertebrates to vertebrates. LPHNs and CELSRs mediate fundamental aspects of brain development, yet CELSR signaling mechanisms are unknown. We find that CELSR1 and CELSR3 are cleavage deficient, while CELSR2 is efficiently cleaved. Despite differential autoproteolysis, CELSR1–3 all engage GαS, and CELSR1 or CELSR3 TA point mutants retain GαS coupling activity. CELSR2 autoproteolysis enhances GαS coupling, yet acute TA exposure alone is insufficient. These studies support that aGPCRs signal via multiple paradigms and provide insights into CELSR biological function.

In brief

Adhesion GPCRs (aGPCRs) control fundamental biological processes by linking extracellular adhesion to intracellular signaling. A predominant model for aGPCR activation involves exposure of a tethered agonist (TA). Bui et al. investigate aGPCR signaling principles by comparing two

*Correspondence: richard.sando@vanderbilt.edu.

AUTHOR CONTRIBUTIONS

D.L.H.B. performed all BRET2 studies, indirect Arr assays, and immunocytochemistry/confocal experiments. A.R., E.O., and R.R. performed all RNA *in situ* experiments. S.J.B. and J.L. conducted CELSR1–3 cleavage assays. D.A. and R.C.S. designed the study with input from all the authors. R.C.S. conducted all molecular cloning and wrote the manuscript with input from all authors.

DECLARATION OF INTERESTS

The authors declare no competing interests.

SUPPLEMENTAL INFORMATION

Supplemental information can be found online at https://doi.org/10.1016/j.celrep.2023.112552.

conserved aGPCR families. Their results support that aGPCRs signal via multiple paradigms in addition to TA exposure.

Graphical Abstract

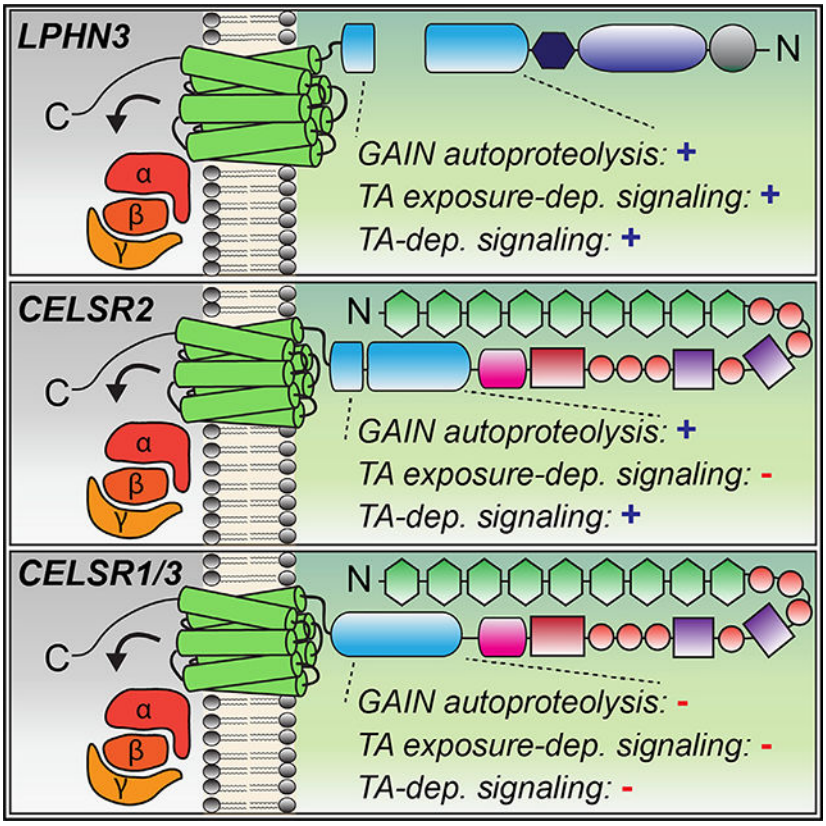

INTRODUCTION

G protein-coupled receptors (GPCRs) are the largest and one of the most evolutionarily diverse membrane protein superfamilies.[1] GPCRs direct multitudes of fundamental biological processes by linking extracellular stimuli to intracellular responses. Adhesion GPCRs (aGPCRs) are a large GPCR class, with 33 members in humans, yet their biological functions and signal transduction mechanisms remain incompletely understood.[2–5] A major obstacle is the lack of a universal understanding of how the aGPCR class is agonized and how they control signaling cascades.[6,7] Virtually all aGPCRs have a GAIN (GPCR autoproteolysis-inducing) domain, which harbors a GPS (GPCR proteolysis site) capable of autoproteolysis, thereby generating an extracellular N-terminal fragment (NTF) and a 7-transmembrane C-terminal fragment (CTF).[8] The most extensively studied activation mechanisms for aGPCRs involve removal or non-covalent attachment of their NTF following autoproteolysis, allowing a membrane-proximal tethered agonist (TA) peptide, also known as the *Stachel* peptide, to agonize the GPCR.[9,10] How universal these TA exposure-dependent or -independent mechanisms of aGPCR activation are across all aGPCRs remains unclear.

Recent structural studies have defined the TA-mediated activation mechanism of several aGPCRs, including latrophilin-3 (LPHN3/ADGRL3), ADGRG1, ADGRG2, ADGRG4, ADGRG5, ADGRD1, and ADGRF1, thereby providing crucial insights into TA-dependent activation.[11–15] Many aGPCRs have displayed important TA-dependent functions, for example ADGRG6 and ADGRD1 in zebrafish.[16] Interestingly, cleavage-independent signaling modes and functions have been previously reported, including evidence for TA exposure in the absence of cleavage.[17] Certain aGPCRs may contain a cleavage-deficient GAIN domain, as previously shown for human BAI3 (brain angiogenesis inhibitor-3).[8] Moreover, ADGRG5 is not efficiently autoproteolyzed yet can still become activated via its TA.[18] GPS motif presence but not cleavage of *C. elegans* LAT-1 is essential for rescuing developmental deficits in lat-1 mutants.[19] An LPHN3 autoproteolysis mutant was capable of rescuing deficits in synapse formation in LPHN3-deficient neurons.[20] Autoproteolysis has been shown to be dispensable for ADGRD1 coupling to Gαs.[21] Autoproteolysis-independent G protein-mediated signaling has also been reported for GPR56/ADGRG1. Namely, synthetic ligands that bind to the extracellular region of ADGRG1 were capable of modulating signaling in ADGRG1 mutants that diminish autoproteolysis.[22] Also, an ADGRG1 mutant lacking a TA exhibited a subset of preserved signaling capabilities, while a BAI1 mutant lacking a TA displayed robust and fully preserved signaling capabilities.[23] Collectively, increasing evidence supports that several distinct modes of signaling including both cleavage-dependent and -independent paradigms exist for aGPCRs. How certain aGPCRs engage these distinct modes to orchestrate specific functions remains poorly understood.

aGPCRs have emerging roles in critical aspects of diverse biological processes. LPHNs and CELSRs (cadherin EGF LAG-repeat 7-transmembrane receptors) are aGPCRs conserved from invertebrate to vertebrates, suggesting that they underlie evolutionarily ancient functions.[24,25] The mammalian LPHNs (LPHN1–3/ADGRL1–3) and their extracellular interaction partners teneurins and FLRTs (fibronectin leucine-rich repeat transmembrane proteins) function in synapse formation and circuit wiring specificity.[20,26–29] LPHNs have also displayed other important roles during early brain development, including neuronal migration.[30] As GPCRs, LPHNs and their invertebrate orthologs have been shown to interact with numerous G protein-dependent pathways. *C. elegans* LPHN ortholog LAT-1 has been shown to interact with a Gαs pathway,[31] while *Drosophila* LPHN ortholog CIRL (calcium-independent receptor for latrotoxin) interacts with a Gαi pathway.[32] In mammals, LPHN1 has displayed interaction with Gαs,[33] Gαi,[33,34] Gαo, and Gαq pathways.[35] LPHN2 is currently less examined but has exhibited coupling to Gαs[36,37] and Gα12/13[38]. LPHN3 has shown several G protein interactions, including Gαs,[15,37,39] Gαi,[15,34,39] Gαq,[15,39,40] and Gα12/13.[11,15,39,40] The G protein-dependent engagement mechanisms and signaling pathways of CELSRs remain unexplored despite their crucial roles in neurodevelopment, although a connection to the RhoA/ROCK (Rho-associated protein kinase) pathway via the planar cell polarity pathway has been illustrated.[41]

Functionally, initial studies found that the *Drosophila* CELSR ortholog starry night (Flamingo) was essential for tissue polarity via Frizzled.[42–44] Seminal neurobiological studies found that Flamingo mutants exhibited disruptions in *Drosophila* visual system topographic maps, suggesting a role in neuronal target selection during circuit assembly.[45,46]

The single *C. elegans* CELSR ortholog Flamingo/cFMI-1 underlies a crucial role in axonal pathfinding and neuronal development.[47,48] cFMI-1 mutants exhibited substantial deficits in GABAergic motorneuron axonal pathfinding, synapse density, and accumulation of synaptic vesicles at non-synaptic regions.[49] cFMI genetically interacts with the Wnt signaling pathway for proper neurite targeting functions.[50,51] In the *Drosophila* nervous system, Flamingo/starry night functions in limiting dendrite extension and promoting axon extension from sensory and motor systems.[52] Important studies showed that *Drosophila* Flamingo functions as a short-range signal to influence growth cone choice of correct postsynaptic partners,[53] supporting a role in circuit wiring. Interestingly, the Flamingo mutant phenotype was partially rescued by a mutant lacking most of the Flamingo extracellular region, suggesting a critical role of the C-terminal 7-transmembrane GPCR.[54] Despite these important previous studies, the biological functions of mammalian CELSR1–3 and how they signal as aGPCRs remain unclear.

Here, we investigate autoproteolytic cleavage and G protein-coupling mechanisms of the aGPCRs CELSR1–3. We combine aGPCR protein engineering approaches to enable acute TA exposure[40,55] with a panel of BRET2 (bioluminescence resonance energy transfer) sensors for the GPCR “transducerome” of 14 different Gαβγ combinations[56] to assess TA exposure-dependent and autoproteolysis-dependent modes of G protein coupling. Furthermore, we determined the differential spatial expression profiles of *Celsr1–3* during postnatal neural circuit assembly. Our results show that different CELSR isoforms induce G proteins in autoproteolysis-dependent or -independent manners and display partially non-overlapping spatial expression patterns during neurodevelopment. These studies reveal insights into how aGPCRs coordinate intracellular signal transduction.

RESULTS

Mammalian CELSR1–3 exhibit distinct autoproteolytic cleavage profiles

Efficient autoproteolysis in the GAIN domain of LPHNs and several other aGPCRs has been well established. However, it remains unclear if CELSRs display autoproteolysis. We first set out to assess the autoproteolytic cleavage events present in *Mus musculus*(*Mm*) full-length CELSR1–3. Multiple sequence alignments showed that *Mm* and *Homo sapiens* CELSR1 and CELSR3 display an unusual GAIN domain compared with other aGPCRs including LPHN1–3, with the catalytic threonine/serine cleavage residue that is part of the typical HL/T or HM/T (the slash denotes a cleavage site) auto-proteolysis sequence replaced with an alanine or glycine, respectively (Figures 1A and 1B). *Mm* and *Homo sapiens* CELSR2 exhibit a GAIN containing the catalytic threonine. The ancestral CELSR ortholog in *C. elegans* (Flamingo/FMI-1) contains a glycine residue at the typical autoproteolytic catalytic region and is more comparable to mammalian CELSR3 (Figure 1B).

We began by cloning full-length *Mm* CELSR1–3, fusing an N-terminal hemagglutinin (HA) tag and a C-terminal FLAG tag to allow detection of the putative NTF and CTF, respectively (Figure 1A). We tested surface vs. total expression in HEK293T cells via immunocytochemistry and found that full-length tagged *Mm* CELSR1–3 were efficiently overexpressed and localized to the surface of HEK293T cells (Figures 1C and 1D). While these high-magnification images comparing surface with total immunolabeling illustrate

the cell surface localization of our tagged full-length constructs, low-magnification images show the distribution of intensities across the cell population (Figures S1A and S1B). We subsequently used these constructs to assay autoproteolytic cleavage of full-length *Mm* CELSR1–3.

We used our tagged full-length *Mm* CELSR1–3 constructs to monitor the putative NTF or CTF resulting from potential autoproteolytic cleavage via HA or FLAG immunoblotting, respectively (Figures 1E, S1C, and S1D). Our experiments included tagged human LPHN3, which is established to be effectively cleaved, as a positive control. When transfected into HEK293T cells, we observed HA and FLAG products corresponding to the predicted sizes of the cleaved NTF and CTF of CELSR2 (Figures 1E, S1C, and S1D). However, N- and C-terminal tagged products for CELSR1 and CELSR3 corresponded predominately to uncleaved, full-length receptors (Figures 1E, S1C, and S1D). Thus, consistent with predictions based on sequence alignments (Figure 1B), full-length *Mm* CELSR1 and CELSR3 are cleavage deficient in their GAIN domain, while full-length CELSR2 displays autoproteolysis.

More extensive multiple sequence alignments of the GAIN region of numerous mammalian and non-mammalian CELSR1 orthologs revealed that the important catalytic autoproteolytic cleavage residue and/or activating phenylalanine important for autoproteolysis and TA-dependent activation have diverged in certain mammalian species (Figure S2). While many mammalian orthologs lack the typical threonine important for GAIN autoproteolysis (i.e., human, mouse, chimp, sheep, rat, and cow), other mammals, including cat and horse, contain this residue (Figure S2A). This suggests that some mammalian CELSR1 orthologs may have diverged to be cleavage deficient, while others may have preserved autoproteolytic cleavage activity. To examine this further, we generated a point mutation in full-length *Mm* CELSR1 to introduce this threonine (CELSR1 A2464T). Similar to our previous experiments, we fused an N-terminal HA tag and a C-terminal FLAG tag to probe for the potential NTF and CTF, respectively, and assessed surface vs. total cell staining. Mutant CELSR1 A2464T was expressed and localized to the surface of HEK293T cells comparable to wild type (WT) (Figures S2B–S2F). Interestingly, introduction of the threonine alone in the A2464T CELSR1 mutant failed to induce robust and efficient autoproteolysis compared with full-length WT *Mm* CELSR1, indicating that the determinants of autoproteolysis extend beyond this single residue (Figure S2G).

Residue T2357 is critical for *Mm* CELSR2 autoproteolysis

Autoproteolysis of *Mm* CELSR2 generates a putative TA peptide, similar to LPHNs. A predicted residue important for autoproteolytic cleavage of CELSR2 based on known cleaved aGPCRs and alignments in Figure 1B is T2357. To determine if this residue is involved, we mutated this threonine to generate two CELSR2 point mutants, T2357A and T2357G, and examined their expression and autoproteolytic cleavage compared with WT CELSR2 and empty vector (Figures 2 and S3). Mutant T2357A and T2357G CELSR2 harbored an N-terminal HA tag and a C-terminal FLAG tag similar to our WT full-length construct. Tagged CELSR2 T2357A and CELSR2 T2357G were expressed on the surface of HEK293T cells at relative levels indistinguishable from WT CELSR2 (Figures 2A–2C

and S3). We then tested these mutant CELSR2 forms in autoproteolysis assays and found that both point mutations diminished autoproteolytic cleavage of *Mm* CELSR2, resulting in predominately a single band via FLAG immunoblotting corresponding to the expected size of the full-length receptor (Figure 2D). Therefore, *Mm* CELSR2 requires residue T2357 for effective GAIN domain autoproteolysis.

Evaluation of aGPCR acute TA exposure-dependent and -independent G protein coupling

Our results support that full-length *Mm* CELSR1 and CELSR3 are cleavage deficient in mammalian cells, while CELSR2 is efficiently cleaved (Figures 1 and 2). The differential mechanisms of cleavage-dependent and -independent aGPCR:G protein coupling and G protein pathways controlled by CELSRs remain unclear. To establish a system to evaluate acute TA-dependent G protein coupling of aGPCRs, we implemented recent advances allowing for acute, thrombin-mediated exposure of the aGPCR TA peptide.[40] We combined the thrombin-mediated acute TA exposure approach with BRET2 sensors (termed TRUPATH) that assay the "transducerome' of 14 Gαβγ combinations (Figures 3 and S4).[56] We validated this approach using LPHN3, as in previous studies.[40] We began by replacing the extracellular portion of *Mm* LPHN3 (NCBI:NM_001359828.1) that is N-terminal of the autoproteolytic cleavage site with PAR (N-terminal domain of protease-activated receptor) (Figures 3A and 3B). This approach allows for overexpression of a TA-protected LPHN3, and subsequent thrombin-mediated cleavage and removal of PAR,[57] which thereby exposes the TA peptide (Figure 3B). Similar to Mathiasen et al.,[40] we fused the PAR sequence to LPHN3 so that thrombin-mediated cleavage in PAR at LDPR/SF would expose the critical activating phenylalanine in the endogenous LPHN3 TA, thereby generating a thrombin-exposed TA of N-SFAVLM ... -C (Figure 3B).

We validated this approach with the TRUPATH sensors for Gα13 (Gα13/Gβ3/Gγ9), which was previously shown to couple LPHN3 in a TA exposure-dependent manner,[40] and GαoB (GαoB/Gβ3/Gγ8) as a negative control. BRET2 experiments were conducted in G protein knockout (GKO) HEK293 cells to minimize interference with endogenous G proteins and our overexpressed receptors of interest (Figure 3C).[58,59] We transfected the same TRUPATH sensors in cells co-transfected with empty vector (EV) to control for non-specific effects of thrombin treatment. Consistent with previous studies,[40] we found thrombin dose-dependent PAR-LPHN3 coupling to Gα13. Importantly, no significant change in net BRET2 was observed in EV conditions treated with similar concentrations of thrombin, supporting that Gα13 coupling was specific for thrombin-mediated cleavage of LPHN3 (Figure 3C). Thus, combining the PAR-LPHN3 approach with TRUPATH sensors provides a system to assess TA-dependent G protein coupling in aGPCRs.

Multiple putative transcript variants are present in public databases for *Mm* LPHN3 in intracellular loop 3 (ICL3), which is important for G protein coupling, as well as the C-terminal intracellular tail sequence, which has been shown to modulate signal transduction pathway specificity for LPHN1.[33] Next, we tested how three putative LPHN3 sequence variants (NCBI transcript variant 5 NM_0013 47371.2, NCBI transcript variant 7 NM_001 359828.1, and NCBI transcript variant 9 NM_001359830.1; here referred to as LPHN3*tv*5, LPHN3*tv*7, and LPHN3*tv*9, respectively) impact G protein coupling (Figures 3D–3L).

Given that several aGPCRs have shown TA exposure-dependent and -independent activity, and LPHN3 has been reported to exhibit both basal and agonist-dependent G protein coupling,[39] we examined basal vs. TA exposure-dependent G protein coupling in parallel. As an initial control to assess potential differences in expression levels of the three PAR-LPHN3 variants tested, we immunolabeled for overexpressed PAR-LPHN3 variants containing a C-terminal HA tag but observed no statistically significant differences (Figures S4A and S4B).

LPHN3*tv*5 exhibits a relatively short ICL3 followed by an intracellular C-terminal tail region with a PDZ-binding motif (Figure 3D). We found that PAR-LPHN3*tv*5 displayed modest basal GαsS coupling and more substantial basal Gα13 coupling in the absence of thrombin-mediated TA exposure (Figure 3E), as well as exposed TA-induced Gα13 coupling (Figure 3F). Further control experiments showed effective agonist-induced (10 μM isoproterenol) coupling of GαsS and GαsL to β2-adrenergic receptor (β2-AR) (Figure S4C), as reported in the TRUPATH study.[56] PAR-LPHN3*tv*7, which contains a 9 amino acid insertion (NYEDNRPFI) in ICL3 compared with LPHN3*tv*5 (Figure 3G), also displayed modest basal and exposure-dependent G protein coupling (Figures 3H and 3I). PAR-LPHN3*tv*9, which contains the same ICL3 as LPHN3*tv*7 but a short C-terminal intracellular tail (Figure 3J), displayed no detectable basal Gα coupling (Figure 3K) but did display robust TA-dependent Gα13 coupling (Figure 3L). To control for other possibilities, such as receptor-induced changes in the expression of TRUPATH sensors, we plotted the donor luminescence measurements from these experiments but found no significant differences between conditions for given sensors (Figure S4D). These experiments further validate these approaches and suggest that aGPCR transcript variants may impact G protein-coupling efficacy.

Given the importance of LPHNs in mechanisms of synapse formation and brain development, we subsequently conducted RNA *in situ* hybridizations with C-terminal variant-specific and pan-*Lphn3* probes at three time points during synaptogenesis. Interestingly, the C-terminal tail present in Lphn3*tv*5 and −7 harbors a PDZ-binding motif that interacts with postsynaptic SHANK proteins.[60] We co-labeled brain sections from postnatal day 5, 10, and 21 mice with a probe detecting all *Lphn3* transcript variants (pan-*Lphn3*) together with a probe specific for the C-terminal tail sequence present in Lphn3*tv5/−7* but not Lphn3*tv9* (Ct-*Lphn3*) (Figures 4 and S5). Probes specific for pan-*Lphn3* as well as the Lphn3*tv5/−7* C-terminal intracellular tail were robustly detected throughout the developing mouse hippocampus (Figure 4A). We quantified the intensities of each probe relative to the area occupied by DAPI and found that Lphn3 expression increased during postnatal development, particularly in the CA1 (Figures 4B and 4C) and CA3 (Figures 4D and 4E) compared with the dentate gyrus (Figures 4F and 4G). The pan-*Lphn3* and Ct-*Lphn3* probes did not completely co-localize in all hippocampal subregions analyzed (Figure S5). The small size of the ICL3 insert sequence precluded similar analyses with this sequence variant, and future studies are required to determine its significance *in vivo*. Altogether, these experiments support that *Lphn3* expression increases in the hippocampus during early postnatal development and that the large C-terminal tail harboring a PDZ-binding motif is highly prevalent during this developmental period.

Full-length CELSR1–3 engage in G protein coupling with GαsS

While autoproteolysis of *Mm* CELSR2 will produce a putative TA peptide, our results support that full-length *Mm* CELSR1 and CELSR3 are cleavage deficient in mammalian cells. This indicates that autoproteolysis-independent modes of signaling may exist for *Mm* CELSR1 and CELSR3. To begin interrogating this, we applied the complete panel of TRUPATH BRET2 sensors to full-length CELSR1–3 to assess G protein coupling (Figures 5 and S6). Given the basal Gα13 coupling we observed upon PAR-LPHN3*tv*5 overexpression, we utilized this as a control within these experiments. Full-length *Mm* CELSR1 displayed GαsS coupling (Figure 5A). Heatmaps illustrate that in these conditions, full-length CELSR1 coupled to GαsS within the panel of TRUPATH sensors (Figure 5B). We subsequently performed plasmid copy number titer experiments where we increased the amount of CELSR1 plasmid transfected together with a given amount of TRUPATH GαsS sensors (Figure 5C). These experiments demonstrated an increasing BRET2 response with increased CELSR1 plasmid copy number compared with EV transfected cells (Figure 5C). Interestingly, similar experiments with full-length *Mm* CELSR2 and CELSR3 also revealed GαsS coupling and plasmid copy-dependent GαsS coupling (Figures 5D–5I). Notably, while a direct comparison has caveats, CELSR2 induced a stronger plasmid copy-dependent GαsS response (Figure 5F) compared with CELSR1 (Figure 5C) or CELSR3 (Figure 5I). Similar to our LPHN3 BRET2 studies, we also analyzed the donor luminescence readings but found no differences between TRUPATH sensors for a given CELSR isoform (Figures S6A–S6C). Altogether, these results support that full-length cleavage-deficient *Mm* CELSR1 and CELSR3 and full-length cleaved CELSR2 engage in G protein coupling with GαsS.

Celsr1–3 are highly abundant during neural circuit assembly and display partially non-overlapping spatial expression patterns

Despite the fundamental importance of the invertebrate CELSR orthologs Flamingo/FMI-1/starry night in circuit assembly, the functions of mammalian CELSR1–3 remain unclear. Thus, we conducted spatial expression analysis of *Mm Celsr1–3* through the developing mouse brain to obtain insights into their *in vivo* roles (Figures 6 and S7). Similar to our *Lphn3* studies, we performed RNA *in situ* hybridizations for *Celsr1–3* at postnatal days 5, 10, and 21, which is a major period of synaptogenesis in the mouse brain. Interestingly, *Celsr1–3* were present in partially non-overlapping spatial patterns during postnatal development, with persistent expression through postnatal day 21 (Figures 6A and S7). We quantified the intensity of each *Celsr* isoform relative to the area occupied by DAPI in the CA1, CA3, and dentate gyrus regions. *Celsr2* and *Celsr3* were the predominant isoforms expressed and were largely restricted to the pyramidal cell layers of the hippocampal CA1/CA3 and granule cell layers of the dentate gyrus (Figures 6B–6G). *Celsr1* was distinct compared with *Celsr2* and *Celsr3*. *Celsr1* was expressed in the hippocampal region at postnatal day 5 but became increasingly restricted to the granule layer of the hippocampal dentate gyrus over development (Figure 6). While *Celsr1* was uniformly distributed throughout the dentate gyrus granule cell layer at postnatal day 5, it became selective for the subgranular zone, where cells responsible for adult neurogenesis reside, by postnatal day 21 (Figures 6F and 6G). Thus, different *Celsr* isoforms display discrete spatial expression patterns, with *Celsr1* and *Celsr2/3* being particularly distinct.

We examined *Celsr2/3* spatial expression more globally by imaging *in situ* hybridizations from sagittal sections and found that *Celsr2* was broadly expressed, while *Celsr3* co-expressed with *Celsr2* in discrete areas including the olfactory bulb, hippocampus, and cerebellum (Figure S7). To determine if *Celsr2/3* expression in hippocampal subregions was enriched in neurons of the pyramidal and granule cell layers, we conducted double immunohistochemistry (IHC)/RNA *in situ* hybridizations for the mature neuronal marker NeuN together with the RNA probes for *Celsr2/3* (Figures 6H and 6I). These experiments revealed that *Celsr2/3* expression overlapped with NeuN in the CA1, CA3, and dentate gyrus (Figures 6H and 6I). Altogether, these studies support that *Celsr1–3* display differential autoproteolysis as well as spatial expression patterns in the developing mouse brain.

Autoproteolysis in the context of full-length *Mm* CELSR2 is important for GαsS coupling

While full-length *Mm* CELSR2 exhibits GαsS coupling properties, CELSR2 autoproteolytic cleavage generates a TA peptide with potential TA exposure-dependent or -independent functions. To first address if autoproteolysis is important for CELSR2:GαsS coupling, we tested the ability of mutant T2357A CELSR2 to couple to GαsS (Figure 7A). We conducted similar plasmid copy-number-dependent GαsS coupling experiments as in Figure 5 and found that the T2357A mutation significantly attenuated GαsS coupling compared with WT CELSR2 (Figure 7A). This supports that efficient *Mm* CELSR2 autoproteolysis enhances its GαsS coupling.

To examine this further, we generated a PAR-CELSR2 construct to allow for acute thrombin-mediated TA exposure (Figures 7B and 7C). We designed PAR-CELSR2 in a similar manner to PAR-LPHN3 by fusing PAR to the CELSR2 CTF so that thrombin-mediated cleavage of PAR at LDPR/S (the slash denotes a cleavage site) would produce the following TA peptide: N-SFAVLM ... -C (Figure 7B). We subsequently examined G protein coupling of PAR-CELSR2, using PAR-LPHN3*tv7* coupling to Gα13 as a control (Figure 7C). Surprisingly, acute CELSR2 TA exposure alone failed to induce G protein coupling including for GαsS or other G proteins (Figure 7C). While Gα12 exhibited modest changes following thrombin treatment, control experiments revealed that thrombin treatment alone in cells transfected with EV can induce the Gα12 TRUPATH BRET2 sensor (Figure S8A). As before, PAR-LPHN3*tv7* displayed strong thrombin-induced Gα13 coupling in the same experiments. Since acute thrombin-mediated TA exposure in PAR-CELSR2 failed to induce G protein coupling in our BRET2 assay, we next tested for arrestin2/3 (Arr-2/3) induction following acute CELSR2 TA exposure using NanoBiT Arr-2/3 membrane recruitment assays (Figures S8B–S8D).[62] Acute CELSR2 TA exposure with the PAR approach also failed to induce Arr-2/3 recruitment (Figures S8C and S8D), supporting a lack of GPCR activation. Altogether, these results suggest that while autoproteolysis is critical for effective *Mm* CELSR2 G protein coupling, acute TA peptide exposure alone using the PAR approach is insufficient for G protein and/or Arr-2/3 induction.

Importantly, the PAR-aGPCR approach generates a “scarred” TA harboring a serine at the N terminus that is not present in the native TA. While this does not interfere with the LPHN3 TA function, it may impact the CELSR2 TA. Therefore, we utilized another acute TA exposure approach recently developed that generates a native exposed TA.[55] This

approach is based on the entirely P′-substrate selectivity of enterokinase, which cleaves following DDDK/.[55] This system has been used to generate functional native exposed TAs for ADGRG6[55] and LPHN3.[61] We adopted this approach for CELSR2 by capping the native CELSR2 TA (N-TSFAVLM ... -C) with SNAP tag-linker-FLAG (Figure 7D). Enterokinase-mediated cleavage in FLAG following DDDK/ exposes the native CELSR2 TA. As a control, we also used a SNAP tag-linker-FLAG-LPHN3*tv7* in parallel. Surface SNAP-tag labeling demonstrated that these fusions were effectively expressed on the cell surface and that enterokinase-cleavage diminished this surface signal, relative to a C-terminal HA tag (Figures 7E and S8E). We subsequently used this system for BRET2 G protein-coupling experiments, including enterokinase (EK)-treated cells transfected with EV and 10 nM ISO-treated cells expressing β2-AR as controls (Figures 7F and 7G). As in Perry-Hauser et al.,[61] this approach effectively induced Gα13 coupling with LPHN3 (Figure 7F). However, consistent with our PAR-CELSR2 experiments (Figures 7B and 7C), acute CELSR2 native TA exposure with this approach failed to induce GαsS coupling (Figure 7G).

These results support that CELSRs may display distinct G protein induction mechanisms compared with LPHN3. To investigate this further, we generated nine point mutations in residues within the CELSR1–3 TA peptide region (Figure 7H). In LPHNs, these residues have shown to be important for autoproteolysis and/or TA-mediated agonism.[8,61] As before, our CELSR1–3 mutations were generated in full-length *Mm* CELSR1–3 displaying N-terminal HA and C-terminal FLAG tags. We first assessed mutant receptor surface localization and autoproteolysis compared with WT forms (Figure S9). CELSR2 F2359A, L2362A, and M2363A mutations impaired autoproteolysis efficiency compared with WT CELSR2 (Figures S9A–S9D). CELSR1 C2466A, L2469A, and M2470A displayed surface levels and an autoproteolysis profile comparable to WT CELSR1 (Figures S9E, S9F, S9I, and S9J). The CELSR3 F2511A mutation significantly diminished surface expression and localization, while CELSR3 L2514A and M2515A were efficiently expressed on the cell surface and exhibited autoproteolysis comparable to WT CELSR3 (Figures S9G–S9J). We subsequently conducted GαsS coupling assays with the mutants that were effectively expressed on the cell surface (Figures 7I–7K). Interestingly, CELSR1 C2466A, L2469A, and M2470A all induced GαsS at a similar intensity to WT CELSR1 (Figure 7I). The three CELSR2 point mutations either abolished (F2359A) or significantly attenuated (L2362A and M2363A) GαsS induction (Figure 7J). However, interpretation of these results in confounded by the observation that these point mutations also impact CELSR2 autoproteolysis. CELSR3 L2514A induced GαsS coupling, while CELSR3 M2515A exhibited a slight reduction in GαsS induction intensity (Figure 7K). Collectively, these results support that these residues are not essential for CELSR1 or CELSR3 GαsS coupling, while CELSR2 requires autoproteolysis in the context of the full-length receptor for robust GαsS induction.

DISCUSSION

Despite the crucial roles of CELSRs in neurodevelopment, how they function as GPCRs remains unknown. Here, we examined aGPCR:G protein induction principles by focusing on mammalian CELSR1–3 and LPHN3, which represent members of evolutionarily conserved aGPCR families shared across invertebrates to vertebrates. We first examined full-length

Mm CELSR1–3 autoproteolysis in a heterologous system and found that CELSR1 and CELSR3 are cleavage deficient, while CELSR2 is cleaved with residue T2357, crucial for efficient autoproteolysis (Figures 1 and 2). We then used an approach to interrogate acute TA exposure-dependent and -independent aGPCR:G protein coupling, first validating this system using *Mm* LPHN3 (Figure 3). Next, we assessed Lphn3 expression together with one C-terminal tail variant in the developing hippocampus and determined that they were highly abundant during postnatal synaptogenesis (Figure 4). Applying the aGPCR:G protein-coupling system to *Mm* CELSR1–3, we found that overexpression of full-length *Mm* CELSR1–3 was sufficient to induce G protein coupling, particularly with GαsS (Figure 5). We then found that *Mm* Celsr1–3 exhibited distinct, non-overlapping spatial expression profiles during neural circuit assembly (Figure 6). Mechanistically, CELSR2 autoproteolysis was important for effective GαsS coupling, yet acute TA exposure alone was insufficient (Figure 7). Also, mutations in the CELSR1 and CELSR3 TA peptide region failed to block GαsS coupling (Figures 7H–7K). Collectively, these results reveal insights into how CELSRs function as aGPCRs and how aGPCRs mediate G protein coupling.

Our study has several inherent limitations that require future experiments to address. First, while even high immunoblot exposures support that the majority of full-length CELSR1 and CELSR3 are uncleaved in our experiments, consistent with their atypical autoproteolysis regions (Figure S1D), we cannot exclude the possibility that a small amount of cleavage product is present. We employed a panel of 14 G protein BRET2 sensors to assess G protein coupling, but we did not examine CELSR downstream signal transduction pathways. Future studies using a range of approaches are required to define the downstream signaling cascades regulated by CELSR1–3 *in vivo*. Moreover, while our studies focused on mammalian CELSRs, the autoproteolysis and G protein-signaling mechanisms of the invertebrate ortholog (cFMI/Flamingo/starry night) remain to be identified. Interestingly, alignments suggest that cFMI-1 may be cleavage deficient (Figure 1B), and thereby more comparable to *Mm* CELSR3, but further experiments are required to address this. The PAR/thrombin-mediated acute TA exposure approach also has certain limitations. The endogenous aGPCR TA peptide is protected within the GAIN domain and is surrounded by numerous hydrogen bonds and hydrophobic interactions. The PAR-aGPCR fusions remove this molecular context and may alter the native TA conformation. However, our results show robust, thrombin-inducible Gα13 coupling to PAR-Lphn3 as in previous studies,[40] further supporting the validity and effectiveness of this approach for acute TA exposure. Development of approaches with enhanced specificity and temporal resolution for inducible TA peptide exposure, such as the EK cleavage strategy, benefit studies of aGPCR signal transduction.

Our results also prompt multiple new questions. We show in a heterologous system that *Mm* CELSR1/3 exhibit a cleavage-deficient GAIN, while CELSR2 is efficiently cleaved. However, full-length CELSR1–3 all engage GαsS, and effective CELSR2 coupling to GαsS requires autoproteolysis. Interestingly, while autoproteolysis is important for CELSR2:GαsS coupling, acute TA exposure alone using the PAR-CELSR2 or EK-CELSR2 approach is insufficient. This contrasts with LPHN3, where acute TA exposure effectively induces Gα13 coupling in the same experiments using the same approaches (Figure 7). This suggests that autoproteolysis is required in the context of the native protein for CELSR2. One

possibility is that the extracellular region plays a crucial role in G protein-coupling induction and therefore acute TA exposure alone is insufficient. Indeed, previous models have been proposed where the extracellular region and 7-transmembrane region communicate, and conformational changes in the extracellular region may directly induce activation without TA exposure.[22,23] Autoproteolysis may be necessary for the conformational changes allowing communication of the CELSR2 extracellular region with the GPCR.

How do cleavage-deficient aGPCRs, such as CELSR1 and CELSR3, induce G protein coupling in the absence of robust autoproteolysis? A model involving the extracellular region may also help explain this. For CELSR1 and CELSR3, the membrane-proximal TA sequence may be still capable of communicating to the 7-transmembrane GPCR via the extracellular region, as shown for other aGPCRs.[17,18] Thus, certain aGPCRs (mouse/human CELSR1 and CELSR3) have acquired mutations over evolution rendering them cleavage deficient yet still capable of inducing G protein coupling. However, a typical TA-dependent mechanism is unlikely for *Mm* CELSR1 and CELSR3 given that mutations in residues important for TA-mediated agonism fail to block GαsS induction (Figures 7H–7K). Unfortunately, we were unable to unequivocally determine the contribution of these residues in CELSR2 toward autoproteolysis-dependent vs. TA-dependent GαsS induction given that point mutations at these sites reduced CELSR2 autoproteolysis (Figures 7J and S9A–S9D). Nonetheless, our studies support that cleavage-independent mechanisms and several modes of signal transduction exist for aGPCRs.

What are the biological roles of CELSR1–3 in the mammalian brain? Critical insights into *C. elegans* and *Drosophila* Flamingo/starry night function have been determined in invertebrate systems, and Flamingo has been associated with the planar cell polarity pathway in development.[41–53] These previous studies support that CELSRs play integral roles in circuit wiring and brain development. Intriguingly, important studies have shown that CELSR2 and CELSR3 modulate opposing roles in mammalian neurite development in cultured neurons.[63] Our studies support differential spatial expression patterns of *Celsr1–3* during neural circuit assembly (Figure 6). These results show that *Celsr2/3* are the predominant isoforms and are expressed in neurons through postnatal life, supporting a neuronal role of *Celsrs* during mammalian postnatal development. *Celsr2/3* also partially overlap in the hippocampus, and therefore we speculate that a cleaved (*Celsr2*) and a cleavage-deficient (*Celsr3*) isoform may have functions in the same cells. Cleavage-deficient *Celsr1* was restricted to early development and persisted in the region responsible for granule cell adult neurogenesis, suggesting a distinct biological role from *Celsr2/3*. Therefore, *Celsr1–3* likely have non-overlapping functions. Our studies elucidating CELSR1–3 autoproteolysis and G protein-coupling mechanisms provide a framework for future studies of CELSR function *in vivo*.

In summary, we investigated autoproteolytic cleavage and Gαs coupling mechanisms of vertebrate *Mm* CELSR1–3. We demonstrated that *Mm* CELSR1–3 display different autoproteolytic cleavage profiles and distinct autoproteolysis-dependent G protein induction paradigms. Thus, aGPCRs exhibit several modes of G protein engagement. Overall, these studies expand our current understanding of aGPCR molecular mechanisms and open avenues of future investigation into CELSR biological function.

Limitations of the study

Here, we utilized a heterologous system to examine full-length mouse CELSR1–3 autoproteolysis upon overexpression in HEK293T cells. We were unable to investigate native mouse CELSR1–3 autoproteolysis in brain tissue due to the lack of reliable antibodies together with lack of CELSR1–3 KO brain homogenate to serve as a control. Future studies are required to determine native CELSR1–3 autoproteolysis *in vivo*.

STAR★METHODS

RESOURCE AVAILABILITY

Lead contact—Further information and requests for resources and reagents should be directed to and will be fulfilled by the lead contact, Richard C. Sando (richard.sando@vanderbilt.edu).

Materials availability—All materials generated in this study will be openly shared upon request free of charge.

Data and code availability—Original Western blot images have been submitted with the manuscript. No original code has been generated in this study. Any additional information required to reanalyze the data reported in this paper is available from the lead contact upon request.

EXPERIMENTAL MODEL AND STUDY PARTICIPANT DETAILS

Animals—Male and female C57/BL6J mice (Jackson Laboratories #664) were weaned at 18–21 days of age and housed in groups of 2–5 on a 12 h light/dark cycle with food and water *ad libidum*. Both genders were used for experimental purposes. Vanderbilt Animal Housing Facility: All procedures conformed to National Institutes of Health Guidelines for the Care and Use of Laboratory Mice and were approved by the Vanderbilt University Administrative Panel on Laboratory Animal Care. Mice for RNA *in situ* studies were euthanized at indicated developmental time-points (postnatal day 5, 10, or 21) and whole brains were flash frozen by indirect exposure to liquid N_2, followed by the procedure for fresh frozen tissue outlined below.

Cell lines—GKO HEK293 cells used for all BRET2 assays were originally a kind gift from Asuka Inoue (Tokyo University, Japan) (Alvarez-Curto et al., 2016; Grundmann et al., 2018); and were provided to our studies as a kind gift from Drs. Vsevolod Gurevich and Chen Zheng. GKO HEK293 cells were maintained in DMEM (Gibco Cat# 11995065) containing 10% FBS (Gibco Cat# 16000044), 1X Penicillin-Streptomycin (Corning Cat# MT30002Cl), and 1x MEM Non-essential Amino Acid (NeA) Solution (Sigma Cat# M7145) at 37°C and 5% CO_2. HEK293 Arrestin2/3 KO used for Indirect Arrestin assays were originally generated by Milligan lab from University of Glasgow (Alvarez-Curto et al., 2016) and were a kind gift from Drs. Vsevolod Gurevich and Chen Zheng (Vanderbilt University). HEK293T cells (ATCC #CRL-11268) were used to examine cDNA overexpression and protein cell surface localization. Cells were maintained in DMEM (Gibco Cat# 11995065) plus 10% FBS (Gibco Cat# 16000044) and 1X Penicillin-

Streptomycin (Corning Cat# MT30002Cl) at 37°C and 5% CO_2 for a maximum of 20 passage numbers.

METHOD DETAILS

Plasmids—All full-length *Mm* CELSR1–3, PAR fusion, and SNAP-FLAG fusion overexpression cDNAs were encoded in the pEB Multi-Neo vector (Wako Chemicals, Japan). All PAR constructs contained an N-terminal fusion of the human thrombin receptor PAR1 signal peptide and PAR cleavage sequence N-MGPRRLLLVAACFSLCGPLLSARTRARRPESKATNATLDPRS-C. PAR-LPHN3 and PAR-CELSR constructs were designed according to Mathiasen et al., 2020. For PAR-LPHN3, the PAR sequence was fused immediately upstream of the tethered agonist sequence beginning at N-FAVLMAH ... -C. Thrombin-mediated cleavage of the PAR at N- … LDPR/S-C (/denotes cleavage site) exposes the following tethered agonist sequence (N-SFAVLMAH ... -C). *Mus musculus* PAR-LPHN3 variants Lphn3*tv*5 (NCBI Reference Sequence NM_001347371.2), Lphn3*tv*7 (NCBI Reference Sequence NM_001359828.1), and Lphn3*tv*9 (NCBI Reference Sequence NM_001359830.1) were cloned into pEB Multi-Neo via gBlocks (Integrated DNA technologies). *Mus musculus* PAR-CELSR2 constructs were based CELSR2 Uniprot #Q9R0M0 and synthesized via codon-optimized gBlock fragments (PAR-CELSR2 amino acids #2359–2919 of *Mm* CELSR2). Full-length *Mm* CELSR1 and *Mm* CELSR2 were cloned from postnatal day 21 mouse brain cDNA library produced in-house using Superscript IV Reverse Transcriptase (Invitrogen #18091050). *Mm* Celsr1 corresponded to NCBI Reference Sequence NM_009886.2 and Uniprot #O35161. *Mm* Celsr2 corresponded to NCBI Reference Sequence NM_017392.4 and Uniprot #Q9R0M0. *Mm* Celsr3 was codon-optimized and synthesized at Gene Universal Inc. (Newark, DE) and corresponded to GenBank #AIJ27736.1. The native signal peptide based on Uniprot was replaced with a preprotrypsin leader and HA tag (N-MSALLILALVGAAVAYPYDVPDYA-C). cDNAs contained the N-terminal preprotrypsin leader-HA and C-terminal FLAG tags. The ADGRL3 construct used as a positive control in cleavage assays consisted of full-length human LPHN3 inserted into pCMV5 using restriction cloning with an N-terminal FLAG tag and an HA tag introduced into the first extracellular loop of the seven-transmembrane region (Lu et al., 2015). The SNAP-FLAG-Lphn3*tv*7 and SNAP-FLAG-CELSR2 constructs contained the following sequence of features fused upstream of the native tethered agonist sequence: IgK signal peptide (METDTLLLW VLLLWVPGSTGDAGAQ) – SNAP-tag – linker (GGSGGSGGS) – FLAG (DYKDDDDK). Enterokinase-mediated cleavage following DDDDK/was designed to expose the native TA sequence for Lphn3*tv*7 (TNFAVLMAH ...) and CELSR2 (TSFAVLMDM ...). Both constructs were cloned into pEB and contained a C-terminal HA-tag fusion. The TRUPATH kit was purchased from Addgene (#1000000163) and was a gift from Bryan Roth. The pcDNA3 FLAG *H. sapiens* beta-2-adrenergic receptor used as a control in BRET2 experiments was a gift from Robert Lefkowitz (Addgene plasmid #14697). *Mm* Arr-2 (NP_796205.1) and *Mm* Arr-3 (NP_001258289.1) were cloned via gBlocks (Integrated DNA technologies) to create N-terminal fusions of SmBiT in pEB-Multi-Neo. *Mm* GRK2 (NP_001277747.1) was cloned from gBlocks (Integrated DNA Technologies) into pEB-Multi-Neo. Cells transfected with empty pEB-Multi-Neo were used

as negative control conditions in all experiments. All molecular cloning was conducted with the In-Fusion Assembly system (Takara #638948).

Antibodies—The following antibodies and reagents were used at the indicated concentrations for immunocytochemistry: anti-HA mouse (Covance Cat# MMS101R; 1:1,000), anti-HA rabbit (Cell Signaling Technologies Cat# 3724; 1:2,000), Alexa Fluor 647 Phalloidin (Invitrogen Cat# A22287; 1:40 diluted in methanol), and corresponding fluorescently-conjugated goat secondary antibodies from Life Technologies (1:1,000). For autoproteolysis assays, anti-FLAG antibody conjugated to iFluor 488 (GenScript A01809) at 1:2,000 dilution, or anti-HA antibody conjugated to iFluor 647 (GenScript A01808) at 1:1,000 were used. For double IHC/RNA *in situ* experiments, anti-NeuN mouse (EMD Millipore #MAB377) was used at a 1:500 dilution and detected with HRP-conjugated goat anti-mouse secondary antibody (Biotium #20400–1mL) at 1:500 together with Opal 520 reagent at 1:1,000 (Akoya Biosciences #OP-001001).

BRET2 assays—HEK G protein K.O cells (Grundmann et al., *Nature Commun.*, 2018) were plated into 12-well plate at a density of 3–4 × 10^5 cells in 1 mL per well. HEK G K.O. media contained 1x DMEM (Gibco Cat# 11995065) plus 10% FBS (Gibco Cat#16000044), 1X Penicillin-Streptomycin (Corning Cat#MT30002Cl) with 1x MEM Non-essential Amino Acid (NeA) Solution (Sigma Cat# M7145). After 16–24 h, cells were co-transfected with receptor of interest and TRUPATH plasmids at 1:1:1:1 DNA ratio (receptor:Gα-R-Luc8:Gβ:Gγ-GFP2) via TransIT-2020 (Mirus Cat# MIR5400). Each condition required 97 μL of room temperature 1x Opti-MEM (Gibco Cat# 31985070), 1 μL each DNA plasmid at 1μg/μL concentration), and 3 μL of room temperature and gently-vortexed TransIT-2020 reagent. The TransIT-2020:DNA complexes mixture were gently mixed via pipetting 10 times and incubated at room temperature for 20 min before adding drop-wise in the well. The plate was rocked gently side to side and incubated at 37°C 24 h before harvesting. In each well, media was aspirated, and cells were washed with 1 mL warm PBS. Cells were detached with 300 μL warm Versene (Gibco Cat# 15040066) and incubated at 37°C for 5 min then resuspended via pipetting 10 times. Cells were plated in complete DMEM containing 1x NeA at 200 μL with a density of 30,000–50,000 cells per well in Matrigel-coated 96-well assay plate. Each experimental condition was plated into three separate wells within the 96-well assay plate. BRET2 assays were performed 48 h after transfection. In each well, media was aspirated and cells were incubated in 80 μL of 1x Hanks' balanced Salt Solution (Gibco Cat# 14175095) with 20 *Mm* HEPES (Sigma Cat# H3375, pH 7.4) and 10 μL 100 μm Coelenterazine-400a (NanoLight Technologies Cat# 340) diluted in PBS for 5 min before adding 10 μL of vehicle solution, isoproterenol agonist (Sigma #I6504), or Thrombin (Sigma Cat# T4648) at 100 U/mL concentration for a final concentration of 10 U/mL, or 10 μL of Thrombin vehicle, which is 0.1% BSA (Roche Cat# 10735086001) in PBS. After 10 min of incubation, BRET intensities were measured via BERTHOLD TriStar^2 LB 942 Multimode Reader with Deep Blue C filter (410nm) and GFP2 filter (515 nm). The BRET ratio was obtained by calculating the ratio of GFP2 signal to Deep Blue C signal per well. The BRET2 ratio of the three wells per condition were then averaged. Net BRET2 was subsequently calculated by subtracting the BRET2 ratio of cells expressing donor only (Gα-RLuc8) from the BRET2 ratio of each respective experimental

condition. Net BRET2 differences were then compared as described in the Figures, by subtracting Net BRET2 ratios of induced (thrombin/isoproterenol) conditions from vehicle treated conditions, or conditions overexpressing indicated receptors compared to empty vector (EV). For plasmid copy-dependent BRET2 experiments, conditions were transfected in a 12-well plate format with the same total amount of plasmid DNA and varying copies of experimental plasmid, adjusted to the same total amount with empty vector (pEB-multi). For Enterokinase treatment BRET2 assays, GKO HEK293 cells were plated and transfected as above. On the day of the assay, media in each well was aspirated and cells were incubated in 80 μL of 1x Hanks' balanced Salt Solution with 20 mM HEPES and 10 μL 100 μm Coelenterazine-400a diluted in PBS for 5 min before adding either 10 μL of 5.5 U of Enterokinase (New England Biolabs #P8070S) in PBS or 10 μL of vehicle PBS. After 15 min incubation, BRET2 intensities were measured as above.

Adhesion GPCR autoproteolysis assays—The autoproteolysis assay was performed similarly to previously described (Araç et al., 2012). HEK293T cells were cultured in Dulbecco's Modified Eagle Medium (Gibco 11965118) + 10% fetal bovine serum (Sigma F0926) at 37°C in a 5% CO_2 atmosphere. At 70% confluency, cells were transfected with 2 μg of either CELSR constructs or empty vector DNA in a 6-well plate (Fisher Scientific FB012927) using a 1:3 mixture of LipoD293 (SignaGen Laboratories SL100668). 48 h later, the cells were washed with 1 mL of Dulbecco's Phosphate Buffered Saline (PBS) (Gibco 14190144) and the PBS was aspirated; dry adhered cells were placed at −80°C. Cells were thawed the following day and the following steps were performed at 4°C: cells were resuspended in a solution of PBS +0.01% bovine serum albumin (BSA) (Sigma A3803) and centrifuged using a swinging-bucket rotor at 2,600 × g for 5 min. The supernatant was aspirated and the cell pellet was resuspended in 500 μL of solubilization buffer (20 mM HEPES pH 7.4, 150 mM NaCl, 2 mM $MgCl_2$ 0.1mM EDTA, 2 mM $CaCl_2$, 1% (v/v) Triton X-100). The resuspended cell pellet was incubated at 4°C with rotation for 30 min for solubilization. The solubilized cell pellet was then centrifuged at 20,000 × g for 15 min and the supernatant was collected as the solubilized cell lysate fraction. Cell lysates were run on 12% SDS-PAGE gels and transferred to 0.45 μm pore nitrocellulose membranes (Bio-Rad 1620251) using a wet transfer system (Bio-Rad) for 1 h at 100 V in a transfer buffer of 24.9 mM Tris-HCl and 193 mM glycine with 20% (v/v) methanol. Either the Kaleidoscope (Bio-Rad 1610375) or the PageRuler Plus (Thermo 26619) protein standards were used. After transfer, the nitrocellulose membrane was blocked for 1 h at room temperature using 4% BSA in TBST (20 mM Tris Base pH 7.4, 150 mM NaCl, 0.1% (v/v) Tween 20). After blocking, membranes were incubated with either anti-FLAG antibody conjugated to iFluor 488 (GenScript A01809) at 1:2,000 dilution, or anti-HA antibody conjugated to iFluor 647 (GenScript A01808) at 1:1,000 dilution overnight at 4°C with gentle rocking. The next day, membranes were washed 4 times with TBST for 5 min each at room temperature. The membranes were imaged at respective wavelengths using the ChemiDoc imaging system (Bio-Rad).

RNA *in situ* hybridizations

Tissue preparation and sectioning: Wild-type C57BL/6J (Jackson #000664) mice were taken from their home cages at postnatal day (P) 5, P10, and P21, and whole brain tissue was

collected in the following manner. Brains were rapidly dissected following brief anesthesia with either ice (P5) or isoflurane (P10 and P21) and placed in a rectangular cryomold (Epredia Peel-a-way #18–30) which was flash-frozen in liquid N_2 for 15 s to allow for indirect exposure of the tissue with liquid N_2. The brain was subsequently embedded in O.C.T. Compound (Fisher Healthcare, #4585) within a second cryomold using a bath of 2-methylbutane (Sigma-Aldrich, #M32631–46) equilibrated with dry ice. Once frozen, the blocks were stored at −80°C until cryosectioning.

The frozen blocks were removed from the −80°C freezer and allowed to sit in the cryostat (Leica CM 1950, #047742456) at −20°C for 1 h to equilibrate. The microtome blade for slicing (Sakura, #4689), forceps (Fine Science Tools), razor blade for block trimming, and paintbrushes for manipulating sections, and the antiroll plate (Leica, #14047742497) were also all placed in the cryostat and allowed to equilibrate. Tissue was sectioned at 15 μm and mounted directly onto room temperature Diamond White Glass microscope slides (Globe Scientific Inc., white frosted 25 × 75 × 1mm, charged +/+, #1358W). Once mounted, the slides were kept in the cryostat until all sectioning was complete. Sections were subsequently dried at −20°C for 1 h, then stored at −80°C.

Tissue Pre-Treatment: The RNAscope Multiplex Fluorescent manual assay (Advanced Cell Diagnostics #323100) was carried out using the Fresh Frozen sample preparation according to the manufacturer's protocol as described below. The RNAscope Hydrogen Peroxide (Advanced Cell Diagnostics, #322335) and RNAscope Protease IV (Advanced Cell Diagnostics, #322336) reagents were set out on the benchtop to equilibrate to room temperature. Sections were removed from the −80°C freezer and placed immediately into ice-cold 4% PFA (Electron Microscopy Sciences, #15714)/PBS (MP Biomedicals, 1 tab/100 mL, #2810306) within a glass slide holder (Epredia RA Lamb Glass Coplin Jar, Fisher #E94). Slides were incubated at 4°C for 15 min to fix the tissue and subsequently washed twice with 1x PBS. Slides were subsequently dehydrated in the following ethanol (Decon Laboratories, Inc., 200 proof, #2705HC) gradient: 50% EtOH/ddH_2O for 5 min, 70% EtOH/ddH_2O for 5 min, followed by two treatments with 100% EtOH (50 mL of each treatment). After the final 100% step, the slides were placed section side up on a paper towel and allowed to air dry for 5 min. Then a hydrophobic pen (IHC World, super pap pen, #SPR0905) was used to draw a barrier around each section, which dried at room temperature for 5 min. While the barriers were drying, the HybEZ Humidity Control Tray with lid (Advanced Cell Diagnostics, #310012) was prepared. A sheet of HybEZ Humidifying Paper (Advanced Cell Diagnostics, #310025) was placed on the bottom of the tray and sprayed with ddH_2O until damp. The EZ-Batch Slide Holder (Advanced Cell Diagnostics, #310017) was placed inside the humidity control tray and the slides were placed in the holder. Three drops of hydrogen peroxide were added to each section. The cover was placed over the humidity control tray and the slides were left to incubate for 10 min at room temperature. Once the incubation was complete, the slides were washed twice with ddH_2O, removing excess liquid after each wash via a vacuum. Slides were reinserted into the slide holder and 4 drops of Protease IV were added to each section, followed by incubation at room temperature for 30 min. While the slides were incubating the RNAscope Probes were prepared in the following manner. First the C2 (Advanced Cell Diagnostics: Mm-Adgrl3-O2-C2 Mus musculus Adhesion G protein-coupled receptor L3 (Adgrl3) transcript variant 7

mRNA, #1046031-C2) and C3 (Advanced Cell Diagnostics, Mm-Adgrl3-C3, #317481-C3) probes and 100 μL/sample of the RNAscope Probe Diluent (Advanced Cell Diagnostics, #300041) were placed in a heat block (Thermo Scientific, #88870003) at 40°C for 10 min, and subsequently removed from the heat and incubated at room temperature for 10 min. The probes were combined to form a probe mix consisting of 100 μL of probe diluent per section, and 2 μL each of the C2 and C3 probes per section, respectively. The HybEZ II Oven (Advanced Cell Diagnostics, #321720) was then pre-warmed to 40°C. Once the Protease IV incubation was complete, the slides were washed twice with 1x PBS, placed back in the slide holder and humidity control tray and 100 μL of probe mix were added to each section. The tray was placed in the HybEZ Oven for 2 h at 40°C to hybridize the probes. While the incubation was occurring, the 1x RNAscope wash buffer solution (Advanced Cell Diagnostics, #310091) and 5x Saline Sodium Citrate (SSC) buffer was prepared. The 20x SSC stock contained175.3 g of NaCl (Fisher Chemical, certified ACS, crystalline, #S271–1) and 88.2 g of sodium citrate (Fisher Chemical, dihydrate, granular, #S279–500) in ddH_2O, pH 7.0. Following the 2-h period slides were washed twice with 1x RNAscope wash buffer and placed in 5x SSC buffer overnight at 4°C.

RNAscope Multiplex Fluorescent Assay: The following reagents were equilibrated at room temperature for 1 h: RNAscope Multiplex FL v2 AMP1 (Advanced Cell Diagnostics, 323101), RNAscope Multiplex FL v2 AMP2 (Advanced Cell Diagnostics, 323102), RNAscope Multiplex FL v2 AMP3 (Advanced Cell Diagnostics, 323103), RNAscope Multiplex FL v2 HRP C1 (Advanced Cell Diagnostics, 323104), RNAscope Multiplex FL v2 HRP C2 (Advanced Cell Diagnostics, 323105), RNAscope Multiplex FL v2 HRP C3 (Advanced Cell Diagnostics, 323106) and RNAscope Multiplex FL v2 HRP Blocker (Advanced Cell Diagnostics, 323107). While this equilibration was occurring, the HybEZ Oven was equilibrated to 40°C. Slides were removed from 5x SSC and washed twice with RNAscope wash buffer. Three drops of the AMP1 were applied to each section and the humidity control tray was placed back in the oven where it incubated for 30 min at 40°C. Slides were subsequently washed twice with wash buffer and placed back in the slide holder and 3 drops of AMP2 were applied to each section and left to incubate in the oven at 40°C for 30 min. Slides were washed twice, and treated with 3 drops of AMP3 at 40°C for 15 min. While the AMP3 incubation was occurring, the dye solutions were prepared as follows. The green and red dyes were prepared at a concentration of 1:1000 by combining 1000 μL of TSA Buffer (Advanced Cell Diagnostics, 322809) with 1 μL of Opal 520 Reagent (in DMSO, Akoya Biosciences, OP-001001) and Opal 570 Reagent (in DMSO, Akoya Biosciences, OP-001003) respectively.

Once the 15-min AMP3 incubation was complete the slides were washed and inserted back into the slide holder, then 3 drops of HRPC1 were applied to each slide, and that was allowed to incubate for 15 min at 40°C. Once that was complete the slides were washed and put back into the slide holder and 3 drops of the HRP Blocker were added to each section. This was allowed to incubate for 15 min at 40°C. Slides were washed and 150 μL of the Opal 570 dye mix was added to each section. This was allowed to incubate at 40°C for 30 min. This process was then repeated for the C3 channel, which was treated with Opal 520 dye.

Counterstaining Mounting and Imaging: Four drops of RNAscope DAPI (Advanced Cell Diagnostics, #323108) were added to each section for the purpose of counterstaining and left to sit at room temperature for 30 s. The DAPI was gently tapped off the slide and 50 μL of Prolong Gold antifade reagent (Invitrogen, #P36930) was added inside the barrier but not directly touching the section, avoiding bubbles. A glass coverslip (Corning, 24 × 60 mm, #2975–246) was lowered onto the slide, slides were allowed to dry overnight in a dark slide box (Fisher Brand, #03–448-4) at 4°C before imaging. Slide boxes were stored in the cold room a 4°C for long term storage. Slides were imaged on a Nikon Eclipse Ti2 Confocal Microscope within 1 week of RNAscope completion. Images were taken at 10x and 60x magnification.

Images were analyzed using NIS-Elements AR 5.41.02 software in the following manner. Using the Automated Measurements and Automated Measurements Results functions, thresholds were assigned to the 405, 488, 561, and 640 channels. This was done using the per channel mode and with the following parameters: (for 405) smooth, clean, separate, and fill holes off, and the size option selected with lower bound of 5 μm; (for 488, 561, and 640) smooth, clean, separate, and fill holes off, no size restrictions. Once the threshold had been set for each channel, the data were exported to excel using the software's built in export feature. The sum intensity for all points for a given channel was found, along with the total pixel area occupied of each channel. Then the sum intensity of each channel was divided by the DAPI area for its respective image to produce a ratio of the sum intensity of the gene-of-interest to the area occupied by internal control DAPI. For each region and postnatal day, 5–10 separate images were analyzed and subsequently averaged to generate an 'n' value for each mouse. Three separate mice were analyzed for each postnatal age, and quantitative data depict the average values from three mice.

Double immunohistochemistry/RNA *in situ* hybridizations—NeuN/RNA *in situ* experiments were conducted in the following manner, essentially as described in the manufacturer's protocol (Advanced Cell Diagnostics #323180 and #323100). Tissue collection, sectioning, and pretreatment was conducted as described above for standard RNA *in situ* experiments up until the initial 10-min room temperature hydrogen peroxide treatment. Following hydrogen peroxide treatment, slides were washed twice with ddH_2O followed by once with 1x-PBS-T (PBS with 0.1% Tween 20). The slides were placed back in the slide holder and 150 μL of the primary antibody (anti-NeuN Mouse, EMD Millipore Corp., #MAB377) diluted in RNAscope Co-Detection Antibody Diluent (Advanced Cell Diagnostics, #323160) in a 1:500 concentration was added to each section. Slides were incubated at 4°C overnight in the humidity control tray. Post-primary Fixation and Protease Treatment: After incubation with the primary antibody, slides were washed three times with 1x-PBS-T at room temperature. Then slides were submerged in 10% Neutral Buffered Formalin (Sigma-Aldrich, #65346–85) for 30 min at room temperature. Following that incubation, slides were washed four times with PBS-T. Slides were subsequently placed back into the humidity control tray, and 4 drops of Protease 4 were added and incubated for exactly 30 min at room temperature. After incubation the slides were washed three times with ddH_2O. The RNAscope Multiplex fluorescent assay was then performed, as described above. Following the last HRP blocker step in the RNAscope Multiplex assay,

immunofluorescence for NeuN was performed. HRP-conjugated goat anti-mouse secondary antibody (Biotium #20400–1mL) was diluted in Co-Detection Antibody Diluent (Advanced Cell Diagnostics, #323160) at a 1:500 concentration was added to completely cover the sections and allowed to incubate at room temperature for 30 min. Slides were subsequently washed twice with 1x PBS-T. Then 150 μL of the previously prepared Opal dye (Akoya Biosciences) was added to the slides and incubated for 10 min at room temperature. Then the slides were washed twice with 1x PBS-T and ready for counterstaining and mounting as described above for standard *in situs*.

Surface labeling and immunocytochemistry—Cover glass (#0, 12 mm, Carolina Biological Supply Company #633009) was placed into 24-well plates and coated for 2 h with 100 μL of 50 μg/mL poly-D-lysine (Gibco #A38904–01) in the 37°C tissue culture incubator. Excess poly-D-lysine was removed, coverslips were washed 3x with sterile ddH_2O, and dried for 30-min. HEK293T cells were plated at 1.5–2 × 10^5 cells/well in 0.5 mL complete DMEM. After 16–24 h, cells were transfected with indicated experimental plasmid via TransIT-2020 (Mirus MIR5400) with a total of 0.5 μg DNA amount/condition/well. After 48-h post-transfection, cells were washed briefly once with PBS, fixed with 4% PFA (Electron Microscopy Science Cat# 15714)/4% sucrose/PBS for 20 min at 4°C, and washed 3 × 5 min in PBS. For surface receptor labeling of HA tag, samples were then transferred directly into blocking buffer (4% BSA (Sigma Cat# 10735086001)/3% goat serum (Jackson Immunoresearch #005000121)/PBS). For total receptor labeling, samples were permeabilized in 0.2% Triton X-100/PBS for 5 min at room temperature and then transferred to blocking buffer. Samples were incubated in blocking buffer for 1 h, and subsequently incubated with diluted primary HA tag antibody (anti-HA rabbit (Cell Signaling Technologies Cat# 3724; 1:2,000)) in blocking buffer for 2 h at room temperature. Samples were then washed 3 × 5 min in PBS, incubated with diluted fluorescently-conjugated secondary antibody (goat anti-rabbit IgG Alexa Fluor 488 Cat#A11032; 1:1,000) together with fluorescently-conjugated Alexa Fluor 647 Phalloidin (Invitrogen Cat# A22287; 1:40 diluted in methanol) and DAPI (Sigma Cat# 10236276001; 1:1,000) in blocking buffer for 30 min, washed three times in PBS, and mounted on UltraClear microscope slides (Denville Scientific Cat# M1021) using 10 μL ProLong Gold antifade reagent (Invitrogen, #P36930) per coverslip. Imaging regions-of-interest were chosen at random. ‘Low-magnification’ images were collected with a 20x objective and ‘high-magnification’ images a 60x objective (see Imaging section for details).

Imaging—Images were acquired using a Nikon A1r resonant scanning Eclipse Ti2 HD25 confocal microscope with a 10x (Nikon #MRD00105, CFI60 Plan Apochromat Lambda, N.A. 0.45), 20x (Nikon #MRD00205, CFI60 Plan Apochromat Lambda, N.A. 0.75), and 60x (Nikon #MRD01605, CFI60 Plan Apochromat Lambda, N.A. 1.4) objectives, operated by NIS-Elements AR v4.5 acquisition software. Laser intensities and acquisition settings were established for individual channels and applied to entire experiments, and images were collected at the following resolution: 10x –1.73 μm/pixel, 20x - 0.62 μm/pixel, 60x - 0.29 μm/pixel. Image analysis was conducted using Nikon Elements, ImageJ, and Adobe Photoshop for Figure purposes. Brightness was adjusted uniformly across all pixels for a given experiment for Figure visualization purposes. Quantification of fluorescence

intensities was conducted by imaging 3–5 image frames per biological replicate, which were averaged to generate a single biological replicate value. The averaged value for each replicate is depicted as open circles in each graph. Cells were selected at random while imaging surface and total receptor labeling in HEK293T cells.

Indirect arrestin assay—The indirect arrestin assay was performed using the NanoBiT membrane recruitment system reported in Spillman et al., 2020. HEK Arrestin 2/3 K.O cells (Alvarez-Curto et al., 2016) were plated into 12-well plate at a density of 3–4 × 10^5 cells in 1 mL per well in 1x DMEM (Gibco Cat# 11995065) plus 10% FBS (Gibco Cat# 16000044) and 1X Penicillin-Streptomycin (Corning Cat# MT30002Cl). After 16–24 h, cells were co-transfected via TransIT-2020 with receptor of interest (0.3 μg/μL); membrane-anchored AG10-CAXX LargeBit (0.05 μg/μL) and β-Arrestin-SmallBit (0.05 μg/μL); *Mm* Grk2 (0.3 μg/μL), and empty vector pEB (0.3 μg/μL) for a total of 1 μg DNA per transfection condition. Each condition required 96 μL of room temperature 1x Opti-MEM (Gibco Cat# 31985070), 1 μL each DNA plasmid at specified concentrations), and 3 μL of room temperature and gently-vortexed TransIT-2020 reagent. The TransIT-2020:DNA complexes mixture were gently mixed via pipetting 10 times and incubated at room temperature for 20 min before adding drop-wise in the well. The plate was rocked gently side to side and incubated at 37°C 24 h before harvesting. In each well, media was aspirated, and cells were washed with 1 mL warm PBS. Cells were detached with 300 μL warm Versene (Gibco Cat# 15040066) and incubated at 37°C for 7 min then resuspended via pipetting 10 times. Cells were transferred to 1.5 mL Eppendorf tube, spun down at 500xg for 5 min, resuspended in 1.5 mL blank 1x DMEM after supernatant were removed, and plated at 70 μL per well in Matrigel-coated 96-well assay plate. Twenty-four hours after plating, cells were treated with 20 μL 1x Nano-Glo Live Cell Substrate (Promega Cat# N2011) diluted in PBS and Arrestin assays were performed. Total luminescence of cells was measured for 0.5 s/well in repeated manner at 42 s cycle length for a total 1 h. Ten μL of ligand (10^{-5} M isoproterenol or Thrombin (Sigma Cat# T4648) at 100 U/mL) or Thrombin vehicle (0.1% BSA (Roche Cat# 10735086001) in PBS) was injected at cycle 15th to reach 100 μL volume in each well.

QUANTIFICATION AND STATISTICAL ANALYSIS

All data are expressed as means ± SEM and represent the results of at least three independent biological replicates, as indicated within each Figure Legend and as open circles within bar graphs. Statistical significance was determined using the two-tailed Student’s t-test, one-way ANOVA, or two-way ANOVA, as indicated in the Figure Legends. Data analysis and statistics were performed with Microsoft Excel, GraphPad Prism 8.0 and GraphPad Prism 9.0.

Supplementary Material

Refer to Web version on PubMed Central for supplementary material.

ACKNOWLEDGMENTS

We thank Drs. Vsevolod Gurevich and Chen Zheng (Vanderbilt University) for kindly sharing GKO HEK293 and Arr-2/3 HEK293 KO cells and for providing essential feedback, guidance, and suggestions on this study. We thank Dr. Asuka Inoue (Tohoku University) for originally providing GKO HEK293 cells. We thank Drs. Ege Kavalali,

Lisa Monteggia, and all members of the Sando laboratory for critical feedback on the manuscript and study. This study was supported by grants from the NIH (R00-MH117235 to R.C.S. and R35-GM148412 to D.A.) and the Sloan Research Fellowship (Alfred P. Sloan Foundation) to R.C.S.

REFERENCES

1. Roth BL, Irwin JJ, and Shoichet BK (2017). Discovery of new GPCR ligands to illuminate new biology. Nat. Chem. Biol. 13, 1143–1151. [PubMed: 29045379]
2. Folts CJ, Giera S, Li T, and Piao X (2019). Adhesion G Protein-Coupled receptors as drug targets for neurological diseases. Trends Pharmacol. Sci. 40, 278–293. [PubMed: 30871735]
3. Morgan RK, Anderson GR, Araç D, Aust G, Balenga N, Boucard A, Bridges JP, Engel FB, Formstone CJ, Glitsch MD, et al. (2019). The expanding functional roles and signaling mechanisms of adhesion G protein-coupled receptors. Ann. N. Y. Acad. Sci. 1456, 5–25. [PubMed: 31168816]
4. Paavola KJ, and Hall RA (2012). Adhesion G protein-coupled receptors: signaling, pharmacology, and mechanisms of activation. Mol. Pharmacol. 82, 777–783. [PubMed: 22821233]
5. Liebscher I, Ackley B, Araç D, Ariestanti DM, Aust G, Bae BI, Bista BR, Bridges JP, Duman JG, Engel FB, et al. (2014). New functions and signaling mechanisms for the class of adhesion G protein-coupled receptors. Ann. N. Y. Acad. Sci. 1333, 43–64. [PubMed: 25424900]
6. Araç D, Sträter N, and Seiradake E (2016). Understanding the structural basis of adhesion GPCR functions. Handb. Exp. Pharmacol. 234, 67–82. [PubMed: 27832484]
7. Vizurraga A, Adhikari R, Yeung J, Yu M, and Tall GG (2020). Mechanisms of adhesion G protein–coupled receptor activation. J. Biol. Chem. 295, 14065–14083. [PubMed: 32763969]
8. Araç D, Boucard AA, Bolliger MF, Nguyen J, Soltis SM, Südhof TC, and Brunger AT (2012). A novel evolutionarily conserved domain of cell-adhesion GPCRs mediates autoproteolysis. EMBO J. 31, 1364–1378. [PubMed: 22333914]
9. Stoveken HM, Hajduczok AG, Xu L, and Tall GG (2015). Adhesion G protein-coupled receptors are activated by exposure of a cryptic tethered agonist. Proc. Natl. Acad. Sci. USA 112, 6194–6199. [PubMed: 25918380]
10. Liebscher I, and Schöneberg T (2016). Tethered agonism: a common activation mechanism of adhesion GPCRs. Handb. Exp. Pharmacol. 234, 111–125. [PubMed: 27832486]
11. Barros-Álvarez X, Nwokonko RM, Vizurraga A, Matzov D, He F, Papasergi-Scott MM, Robertson MJ, Panova O, Yardeni EH, Seven AB, et al. (2022). The tethered peptide activation mechanism of adhesion GPCRs. Nature 604, 757–762. [PubMed: 35418682]
12. Ping YQ, Xiao P, Yang F, Zhao RJ, Guo SC, Yan X, Wu X, Zhang C, Lu Y, Zhao F, et al. (2022). Structural basis for the tethered peptide activation of adhesion GPCRs. Nature 604, 763–770. [PubMed: 35418678]
13. Qu X, Qiu N, Wang M, Zhang B, Du J, Zhong Z, Xu W, Chu X, Ma L, Yi C, et al. (2022). Structural basis of tethered agonism of the adhesion GPCRs ADGRD1 and ADGRF1. Nature 604, 779–785. [PubMed: 35418679]
14. Xiao P, Guo S, Wen X, He QT, Lin H, Huang SM, Gou L, Zhang C, Yang Z, Zhong YN, et al. (2022). Tethered peptide activation mechanism of the adhesion GPCRs ADGRG2 and ADGRG4. Nature 604, 771–778. [PubMed: 35418677]
15. Qian Y, Ma Z, Liu C, Li X, Zhu X, Wang N, Xu Z, Xia R, Liang J, Duan Y, et al. (2022). Structural insights into adhesion GPCR ADGRL3 activation and Gq, Gs, Gi, and G12 coupling. Mol. Cell 82, 4340–4352.e6. [PubMed: 36309016]
16. Liebscher I, Schön J, Petersen SC, Fischer L, Auerbach N, Demberg LM, Mogha A, Cöster M, Simon KU, Rothemund S, et al. (2014). A tethered agonist within the ectodomain activates the adhesion G protein-coupled receptors GPR126 and GPR133. Cell Rep. 9, 2018–2026. [PubMed: 25533341]
17. Beliu G, Altrichter S, Guixà-González R, Hemberger M, Brauer I, Dahse AK, Scholz N, Wieduwild R, Kuhlemann A, Batebi H, et al. (2021). Tethered agonist exposure in intact adhesion/class B2 GPCRs through intrinsic structural flexibility of the GAIN domain. Mol. Cell 81, 905–921.e5. [PubMed: 33497605]

18. Wilde C, Fischer L, Lede V, Kirchberger J, Rothemund S, Schöneberg T, and Liebscher I (2016). The constitutive activity of the adhesion GPCR GPR114/ADGRG5 is mediated by its tethered agonist. Faseb. J. 30, 666–673. [PubMed: 26499266]
19. Prömel S, Frickenhaus M, Hughes S, Mestek L, Staunton D, Woollard A, Vakonakis I, Schöneberg T, Schnabel R, Russ AP, and Langenhan T (2012). The GPS motif is a molecular switch for bimodal activities of adhesion class G protein-coupled receptors. Cell Rep. 2, 321–331. [PubMed: 22938866]
20. Sando R, Jiang X, and Südhof TC (2019). Latrophilin GPCRs direct synapse specificity by coincident binding of FLRTs and teneurins. Science 363, eaav7969. [PubMed: 30792275]
21. Bohnekamp J, and Schöneberg T (2011). Cell adhesion receptor GPR133 couples to Gs protein. J. Biol. Chem. 286, 41912–41916. [PubMed: 22025619]
22. Salzman GS, Zhang S, Gupta A, Koide A, Koide S, and Araç D (2017). *Stachel*-independent modulation of GPR56/ADGRG1 signaling by synthetic ligands directed to its extracellular region. Proc. Natl. Acad. Sci. USA 114, 10095–10100. [PubMed: 28874577]
23. Kishore A, Purcell RH, Nassiri-Toosi Z, and Hall RA (2016). Stalk-dependent and stalk-independent signaling by the adhesion G protein-coupled receptors GPR56 (ADGRG1) and Bai1 (ADGRB1). J. Biol. Chem. 291, 3385–3394. [PubMed: 26710850]
24. Boutin C, Goffinet AM, and Tissir F (2012). Celsr1–3 cadherins in PCP and brain development. Curr. Top. Dev. Biol. 101, 161–183. [PubMed: 23140629]
25. Goffinet AM, and Tissir F (2017). Seven pass cadherins CELSR1–3. Semin. Cell Dev. Biol. 69, 102–110. [PubMed: 28716607]
26. Anderson GR, Maxeiner S, Sando R, Tsetsenis T, Malenka RC, and Südhof TC (2017). Postsynaptic aGPCR Latrophilin–2 mediates target recognition in entorhinal–hippocampal synapse assembly. J. Cell Biol. 216, 3831–3846. [PubMed: 28972101]
27. Berns DS, DeNardo LA, Pederick DT, and Luo L (2018). Teneurin-3 controls topographic circuit assembly in the hippocampus. Nature 554, 328–333. [PubMed: 29414938]
28. O'Sullivan M, de Wit J, Savas JN, Comoletti D, Otto-Hitt S, Yates JR 3rd, and Ghosh A (2012). FLRT proteins are endogenous latrophilin ligands and regulate excitatory synapse development. Neuron 73, 903–910. [PubMed: 22405201]
29. Zhang X, Lin PY, Liakath-Ali K, and Südhof TC (2022). Teneurins assemble into presynaptic nanoclusters that promote synapse formation via post-synaptic non-teneurin ligands. Nat. Commun. 13, 2297. [PubMed: 35484136]
30. Del Toro D, Carrasquero-Ordaz MA, Chu A, Ruff T, Shahin M, Jackson VA, Chavent M, Berbeira-Santana M, Seyit-Bremer G, Brignani S, et al. (2020). Structural basis of teneurin-latrophilin interaction in repulsive guidance of migrating neurons. Cell 180, 323–339.e19. [PubMed: 31928845]
31. Müller A, Winkler J, Fiedler F, Sastradihardja T, Binder C, Schnabel R, Kungel J, Rothemund S, Hennig C, Schöneberg T, and Prömel S (2015). Oriented cell division in the C. elegans embryo is coordinated by G protein signaling dependent on the adhesion GPCR LAT-1. PLoS Genet. 11, e1005624. [PubMed: 26505631]
32. Scholz N, Guan C, Nieberler M, Grotemeyer A, Maiellaro I, Gao S, Beck S, Pawlak M, Sauer M, Asan E, et al. (2017). Mechano-dependent signaling by latrophilin/CIRL quenches cAMP in proprioceptive neurons. Elife 6, e28360. [PubMed: 28784204]
33. Ovando-Zambrano JC, Arias-Montaño JA, and Boucard AA (2019). Alternative splicing event modifying ADGRL1/latrophilin-1 cytoplasmic tail promotes both opposing and dual cAMP signaling pathways. Ann. N. Y. Acad. Sci. 1456, 168–185. [PubMed: 31339586]
34. Nazarko O, Kibrom A, Winkler J, Leon K, Stoveken H, Salzman G, Merdas K, Lu Y, Narkhede P, Tall G, et al. (2018). A comprehensive mutagenesis screen of the adhesion GPCR Latrophilin-1/ADGRL1. iScience 3, 264–278. [PubMed: 30428326]
35. Lelianova VG, Davletov BA, Sterling A, Rahman MA, Grishin EV, Totty NF, and Ushkaryov YA (1997). Alpha-latrotoxin receptor, latrophilin, is a novel member of the secretin family of G protein-coupled receptors. J. Biol. Chem. 272, 21504–21508. [PubMed: 9261169]

36. Camillo C, Facchinello N, Villari G, Mana G, Gioelli N, Sandri C, Astone M, Tortarolo D, Clapero F, Gays D, et al. (2021). LPHN2 inhibits vascular permeability by differential control of endothelial cell adhesion. J. Cell Biol. 220, e202006033. [PubMed: 34581723]
37. Sando R, and Südhof TC (2021). Latrophilin GPCR signaling mediates synapse formation. Elife 10, e65717. [PubMed: 33646123]
38. Pederick DT, Perry-Hauser NA, Meng H, He Z, Javitch JA, and Luo L (2023). Context-dependent requirement of G protein coupling for Latrophilin-2 in target selection of hippocampal axons. eLife 12, e83529. [PubMed: 36939320]
39. Moreno-Salinas AL, Holleran BJ, Ojeda-Muñiz EY, Correoso-Braña KG, Ribalta-Mena S, Ovando-Zambrano JC, Leduc R, and Boucard AA (2022). Convergent selective signaling impairment exposes the pathogenicity of latrophilin-3 missense variants linked to inheritable ADHD susceptibility. Mol. Psychiatry 27, 2425–2438. [PubMed: 35393556]
40. Mathiasen S, Palmisano T, Perry NA, Stoveken HM, Vizurraga A, McEwen DP, Okashah N, Langenhan T, Inoue A, Lambert NA, et al. (2020). G12/13 is activated by acute tethered agonist exposure in the adhesion GPCR ADGRL3. Nat. Chem. Biol. 16, 1343–1350. [PubMed: 32778842]
41. Nishimura T, Honda H, and Takeichi M (2012). Planar cell polarity links axes of spatial dynamics in neural-tube closure. Cell 149, 1084–1097. [PubMed: 22632972]
42. Chae J, Kim MJ, Goo JH, Collier S, Gubb D, Charlton J, Adler PN, and Park WJ (1999). The Drosophila tissue polarity gene starry night encodes a member of the protocadherin family. Development 126, 5421–5429. [PubMed: 10556066]
43. Lu B, Usui T, Uemura T, Jan L, and Jan YN (1999). Flamingo controls the planar polarity of sensory bristles and asymmetric division of sensory organ precursors in Drosophila. Curr. Biol. 9, 1247–1250. [PubMed: 10556092]
44. Usui T, Shima Y, Shimada Y, Hirano S, Burgess RW, Schwarz TL, Takeichi M, and Uemura T (1999). Flamingo, a seven-pass transmembrane cadherin, regulates planar cell polarity under the control of Frizzled. Cell 98, 585–595. [PubMed: 10490098]
45. Lee RC, Clandinin TR, Lee CH, Chen PL, Meinertzhagen IA, and Zipursky SL (2003). The protocadherin Flamingo is required for axon target selection in the Drosophila visual system. Nat. Neurosci. 6, 557–563. [PubMed: 12754514]
46. Senti KA, Usui T, Boucke K, Greber U, Uemura T, and Dickson BJ (2003). Flamingo regulates R8 axon-axon and axon-target interactions in the Drosophila visual system. Curr. Biol. 13, 828–832. [PubMed: 12747830]
47. Loveless T, and Hardin J (2012). Cadherin complexity: recent insights into cadherin superfamily function in C. elegans. Curr. Opin. Cell Biol. 24, 695–701. [PubMed: 22819515]
48. Steimel A, Wong L, Najarro EH, Ackley BD, Garriga G, and Hutter H (2010). The flamingo ortholog FMI-1 controls pioneer-dependent navigation of follower axons in C. elegans. Development 137, 3663–3673. [PubMed: 20876647]
49. Najarro EH, Wong L, Zhen M, Carpio EP, Goncharov A, Garriga G, Lundquist EA, Jin Y, and Ackley BD (2012). Caenorhabditis elegans flamingo cadherin fmi-1 regulates GABAergic neuronal development. J. Neurosci. 32, 4196–4211. [PubMed: 22442082]
50. Ackley BD (2013). C. elegans fmi-1/flamingo and Wnt pathway components interact genetically to control the anteroposterior neurite growth of the VD GABAergic neurons. Worm 2, e25715. [PubMed: 24778938]
51. Huarcaya Najarro E, and Ackley BD (2013). C. elegans fmi-1/flamingo and Wnt pathway components interact genetically to control the anteroposterior neurite growth of the VD GABAergic neurons. Dev. Biol. 377, 224–235. [PubMed: 23376536]
52. Mrkusich EM, Flanagan DJ, and Whitington PM (2011). The core planar cell polarity gene prickle interacts with flamingo to promote sensory axon advance in the Drosophila embryo. Dev. Biol. 358, 224–230. [PubMed: 21827745]
53. Chen PL, and Clandinin TR (2008). The cadherin Flamingo mediates level-dependent interactions that guide photoreceptor target choice in Drosophila. Neuron 58, 26–33. [PubMed: 18400160]
54. Steinel MC, and Whitington PM (2009). The atypical cadherin Flamingo is required for sensory axon advance beyond intermediate target cells. Dev. Biol. 327, 447–457. [PubMed: 19146847]

55. Lizano E, Hayes JL, and Willard FS (2021). A synthetic method to assay adhesion-family G protein coupled receptors. Determination of the G protein coupling profile of ADGRG6 (GPR126). Biochem. Biophys. Res. Commun. 534, 317–322. [PubMed: 33248691]

56. Olsen RHJ, Diberto JF, English JG, Glaudin AM, Krumm BE, Slocum ST, Che T, Gavin AC, McCorvy JD, Roth BL, and Strachan RT (2020). TRUPATH, an open-source biosensor platform for interrogating the GPCR transducerome. Nature Chem. Biol. 16, 841–849. [PubMed: 32367019]

57. Vu TK, Hung DT, Wheaton VI, and Coughlin SR (1991). Molecular cloning of a functional thrombin receptor reveals a novel proteolytic mechanism of receptor activation. Cell 64, 1057–1068. [PubMed: 1672265]

58. Alvarez-Curto E, Inoue A, Jenkins L, Raihan SZ, Prihandoko R, Tobin AB, and Milligan G (2016). Targeted elimination of G proteins and arrestins defines their specific contributions to both intensity and duration of G protein-coupled receptor signaling. J. Biol. Chem. 291, 27147–27159. [PubMed: 27852822]

59. Grundmann M, Merten N, Malfacini D, Inoue A, Preis P, Simon K, Rüttiger N, Ziegler N, Benkel T, Schmitt NK, et al. (2018). Lack of beta-arrestin signaling in the absence of active G proteins. Nat. Commun. 9, 341. [PubMed: 29362459]

60. Tobaben S, Südhof TC, and Stahl B (2000). The G protein-coupled receptor CL1 interacts directly with proteins of the shank family. J. Biol. Chem. 275, 36204–36210. [PubMed: 10958799]

61. Perry-Hauser NA, VanDyck MW, Lee KH, Shi L, and Javitch JA (2022). Disentangling autoproteolytic cleavage from tethered agonist-dependent activation of the adhesion receptor ADGRL3. J. Biol. Chem. 298, 102594. [PubMed: 36244455]

62. Spillmann M, Thurner L, Romantini N, Zimmermann M, Meger B, Behe M, Waldhoer M, Schertler GFX, and Berger P (2020). New insights into arrestin recruitment to GPCRs. Int. J. Mol. Sci. 21, 4949. [PubMed: 32668755]

63. Shima Y, Kawaguchi S.y., Kosaka K, Nakayama M, Hoshino M, Nabeshima Y, Hirano T, and Uemura T (2007). Opposing roles in neurite growth control by two seven-pass transmembrane cadherins. Nat. Neurosci. 10, 963–969. [PubMed: 17618280]

64. Lu YC, Nazarko OV, Sando R, Salzman GS, Li NS, Sudhof TC, and Arac D (2015). Structural basis of Latrophilin-FLRT-UNC5 interaction in cell adhesion. Structure 23, 1678–1691. [PubMed: 26235030]

Highlights

- CELSR1 and CELSR3 are cleavage-deficient aGPCRs, while CELSR2 is cleavage competent
- Despite differential GAIN autoproteolytic cleavage, CELSR1–3 all induce Gαs coupling
- Cleavage enhances CELSR2:Gαs coupling, while tethered agonist exposure is insufficient
- CELSR1 and CELSR3 tethered agonist mutants retain G protein-coupling capability

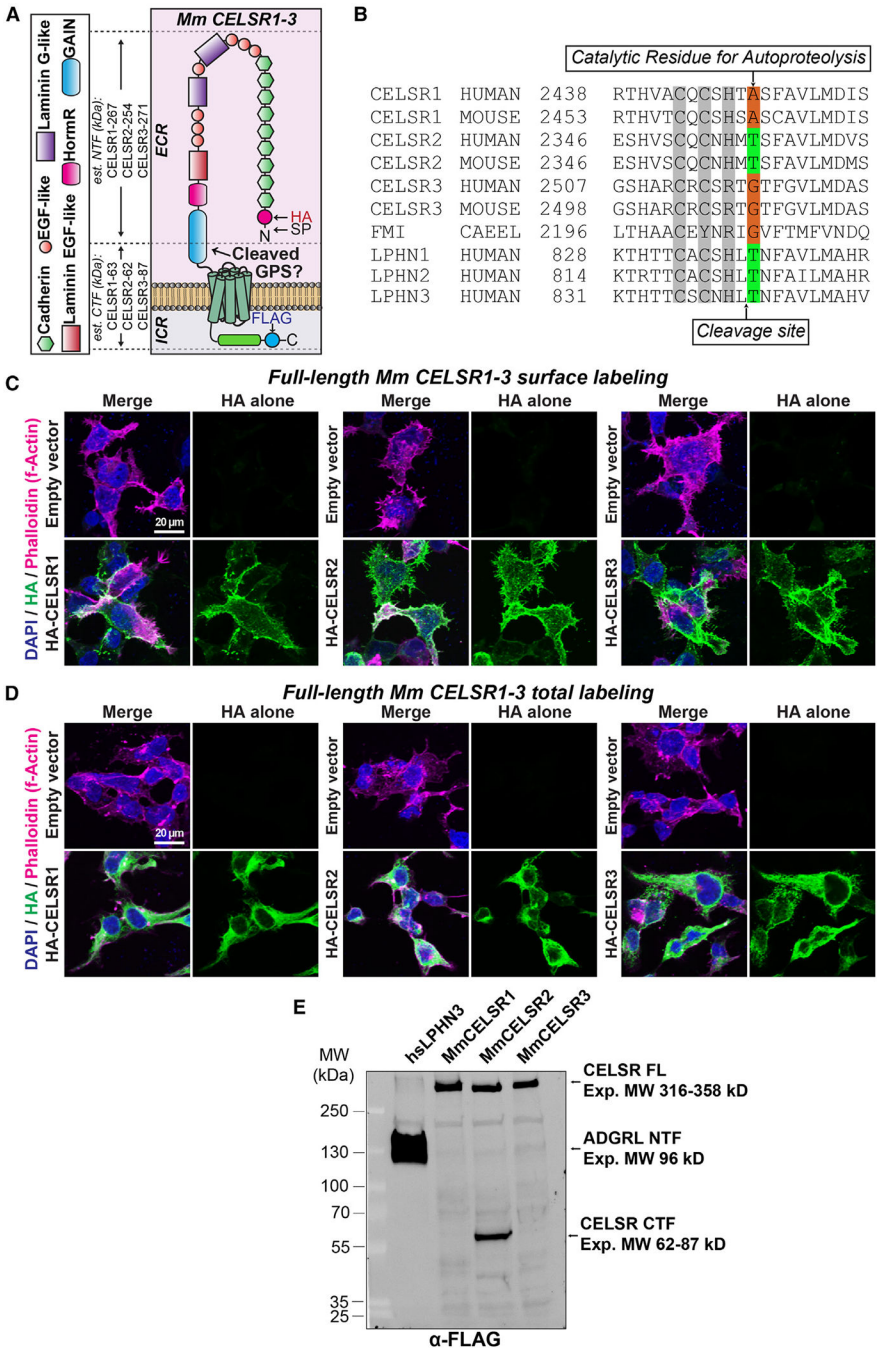

Figure 1. *Mm* CELSR1–3 display distinct autoproteolytic cleavage profiles

(A) Diagram of full-length *Mus musculus* (*Mm*) CELSR1–3 depicting locations of N-terminal HA and C-terminal FLAG tags. The estimated molecular weight of the N-terminal fragment (NTF) and C-terminal fragment (CTF) that would result from cleavage is shown on the left. ECR, extracellular region; ICR, intracellular region; EGF, epidermal growth factor; HormR, hormone receptor domain; GAIN, G protein-coupled receptor autoproteolysis-inducing domain; SP, signal peptide; GPS, G protein-coupled receptor proteolysis site.

(B) Multiple sequence alignment of the GAIN region of human, mouse, and *C. elegans* (CAEEL) CELSR (FMI-1) compared with human Lphn1–3 (Adgrl1–3). The autoproteolytic cleavage site is shown with an arrow on the bottom of the alignment, while the residue critical for autoproteolysis is depicted on the top of the alignment.
(C) Surface expression and localization of full-length *Mm* CELSR1–3 in HEK293T cells. Cells were transfected with indicated full-length HA-tagged *Mm* CELSR constructs or empty vector and immunolabeled for surface HA in unpermeabilized conditions, followed by phalloidin (F-actin) and DAPI.
(D) Total expression of full-length *Mm* CELSR1–3. Similar to (C) except that HEK293T cells were permeabilized and labeled for total HA together with phalloidin and DAPI.
(E) Full-length *Mm* CELSR1–3 cleavage assays in HEK293T cells. Constructs contained N-terminal HA and C-terminal FLAG tags. Full-length *Mm* CELSR2 generates a cleaved C-terminal product at the expected size following autoproteolytic cleavage, while CELSR1/3 is uncleaved under similar conditions. Human LPHN3 was used as a positive control. Expected sizes (kDa): *Mm* CELSR1 full length (FL): 330, NTF: 267, and CTF: 63; *Mm* CELSR2 FL: 316, NTF: 254, and CTF: 62; *Mm* CELSR3 FL: 359, NTF: 271, and CTF: 87; *Homo sapiens* (*hs*) LPHN3 FL: 166, NTF: 96, and CTF: 70. Note that for the *hs* LPHN3 positive control, the FLAG tag was present on the NTF. The presence of two bands in *hs* LPHN3 is likely due to glycosylation (Araç et al.[8]).
See Figures S1 and S2 for additional full-length *Mm* CELSR1–3 autoproteolysis data.

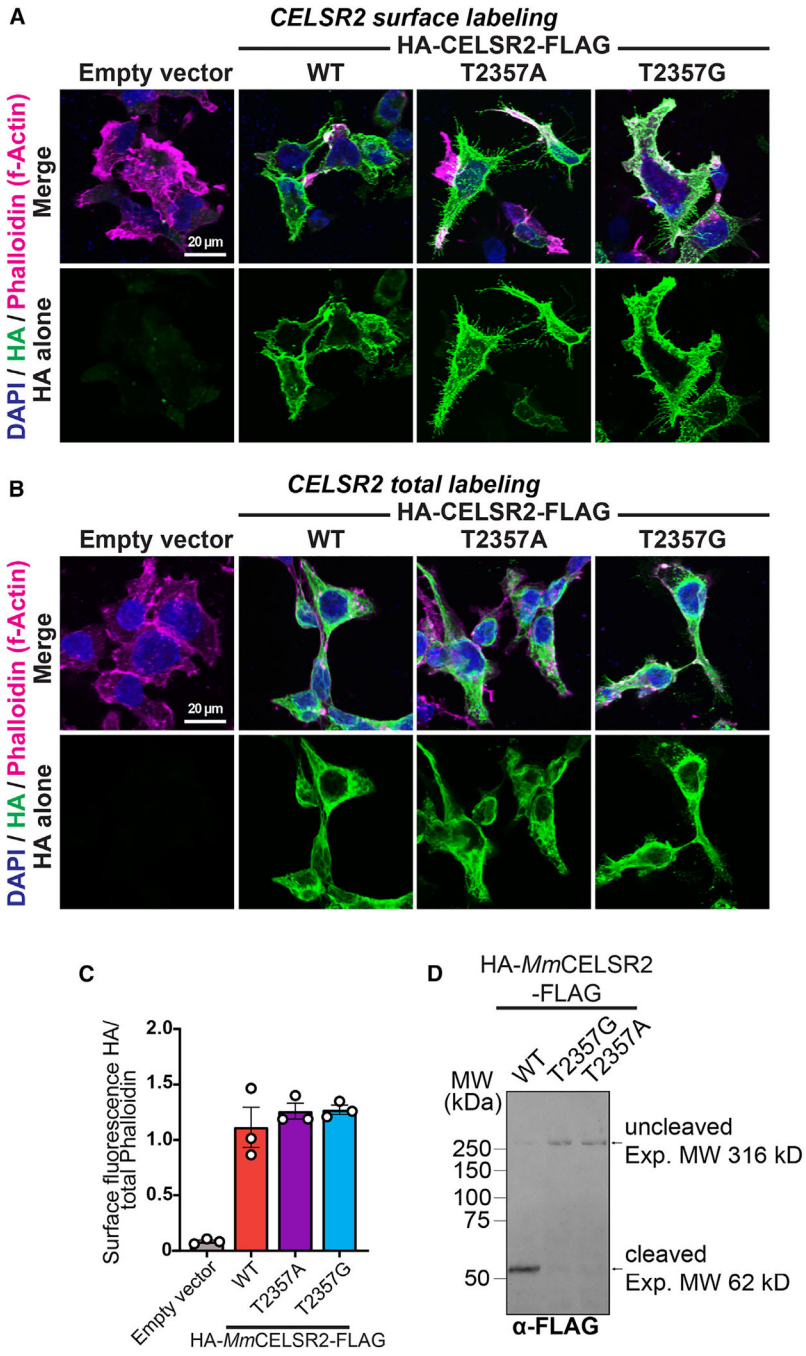

Figure 2. T2357 is important for *Mm* CELSR2 autoproteolysis

(A) Representative images of surface expression levels of full-length *Mm* CELSR2 relative to CELSR2 point mutants (T2357A and T2357G). HEK293T cells were transfected with indicated full-length HA-*Mm* CELSR2-FLAG constructs (WT or indicated point mutants) or empty vector and immunolabeled for surface HA in unpermeabilized conditions, followed by phalloidin (F-actin) and DAPI (nuclei).

(B) Total expression of indicated constructs. Similar to (A) except that HEK293T cells were permeabilized and labeled for total HA together with phalloidin and DAPI.

(C) Quantification of HA surface intensity relative to phalloidin. Total cell fluorescence was measured for HA and phalloidin channels from three independent culture replicates.
(D) *Mm* CELSR2 cleavage assays. HEK293T cells were transfected with the indicated HA-*Mm* CELSR2-FLAG constructs and subsequently immunoblotted for the C-terminal FLAG-tagged cleavage product. Numerical data are means ± SEM from 3 independent biological replicates (depicted as open circles). See Figure S3 for additional data regarding *Mm* CELSR2 autoproteolysis.

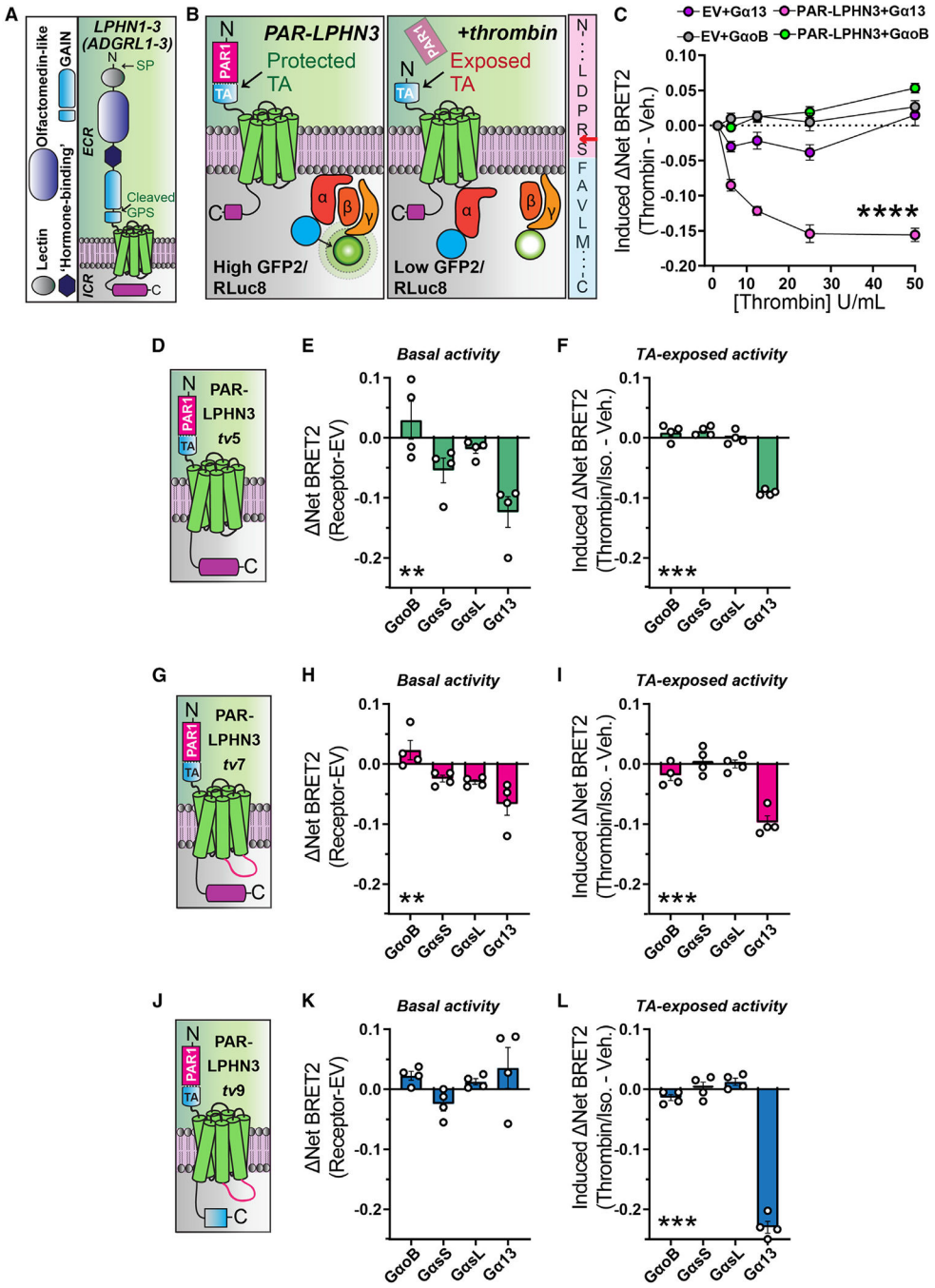

Figure 3. Validation of BRET2 approach to evaluate TA exposure-dependent and -independent aGPCR:G protein coupling

(A) Diagram of *Mm* LPHN1–3 (ADGRL1–3) domain organization. LPHNs exhibit a cleaved GAIN domain, which exposes a TA peptide. ECR, extracellular region; ICR, intracellular region; GAIN, G protein-coupled receptor autoproteolysis-inducing domain; SP, signal peptide; GPS, G protein-coupled receptor proteolysis site.

(B) Model of experimental approach for acute TA exposure and subsequent BRET2 measurements of G protein coupling. Left, replacement of the LPHN3 ECD with PAR protects the TA from inducing TA-dependent G protein induction. Middle, thrombin-

mediated cleavage and removal of PAR exposes the TA, resulting in TA-dependent activation generating a decrease in BRET2 ratio. Right, illustration of PAR-LPHN3 TA cleavage site. Thrombin cleaves PAR (pink sequence) following arginine (red arrow), exposing an N-terminal serine followed by the activating phenylalanine present in the LPHN3 TA sequence (light blue sequence).

(C) Thrombin-mediated LPHN3 TA exposure induces Gα13 coupling using TRUPATH G protein sensors. Transfected cells were subjected to increasing concentrations of thrombin for 10 min followed by BRET2 measurements.

(D) Schematic diagram of PAR-LPHN3*tv*5 (NCBI: NM_001347371.2).

(E) Basal G protein coupling of PAR-LPHN3*tv*5 using the indicated set of TRUPATH BRET2 sensors.

(F) PAR-LPHN3*tv*5 TA-exposure-dependent G protein coupling.

(G) Schematic diagram of PAR-LPHN3*tv*7 (NCBI: NM_001359828.1).

(H) Same as (E) except for PAR-LPHN3*tv*7.

(I) Same as (F) except for PAR-LPHN3*tv*7.

(J) Schematic diagram of PAR-LPHN3*tv*9 (NCBI: NM_001359830.1). LPHN3*tv*9 contains the same intracellular loop 3 as LPHN3*tv*7 but differs from LPHN3*tv*5 and LPHN3*tv*7 by exhibiting a distinct, shorter intracellular tail sequence.

(K) Same as (E) except for PAR-LPHN3*tv*9.

(L) Same as (F) except for PAR-LPHN3*tv*9.

Numerical data are means ± SEM from four independent biological replicates (depicted as open circles in bar graphs). Statistical significance was assessed by two-way ANOVA (****$p < 0.0001$) in (C) and one-way ANOVA for remaining panels (**$p < 0.01$; ***$p < 0.001$). Asterisks depict ANOVA results.

See Figure S4 for additional PAR-LPHN3 data.

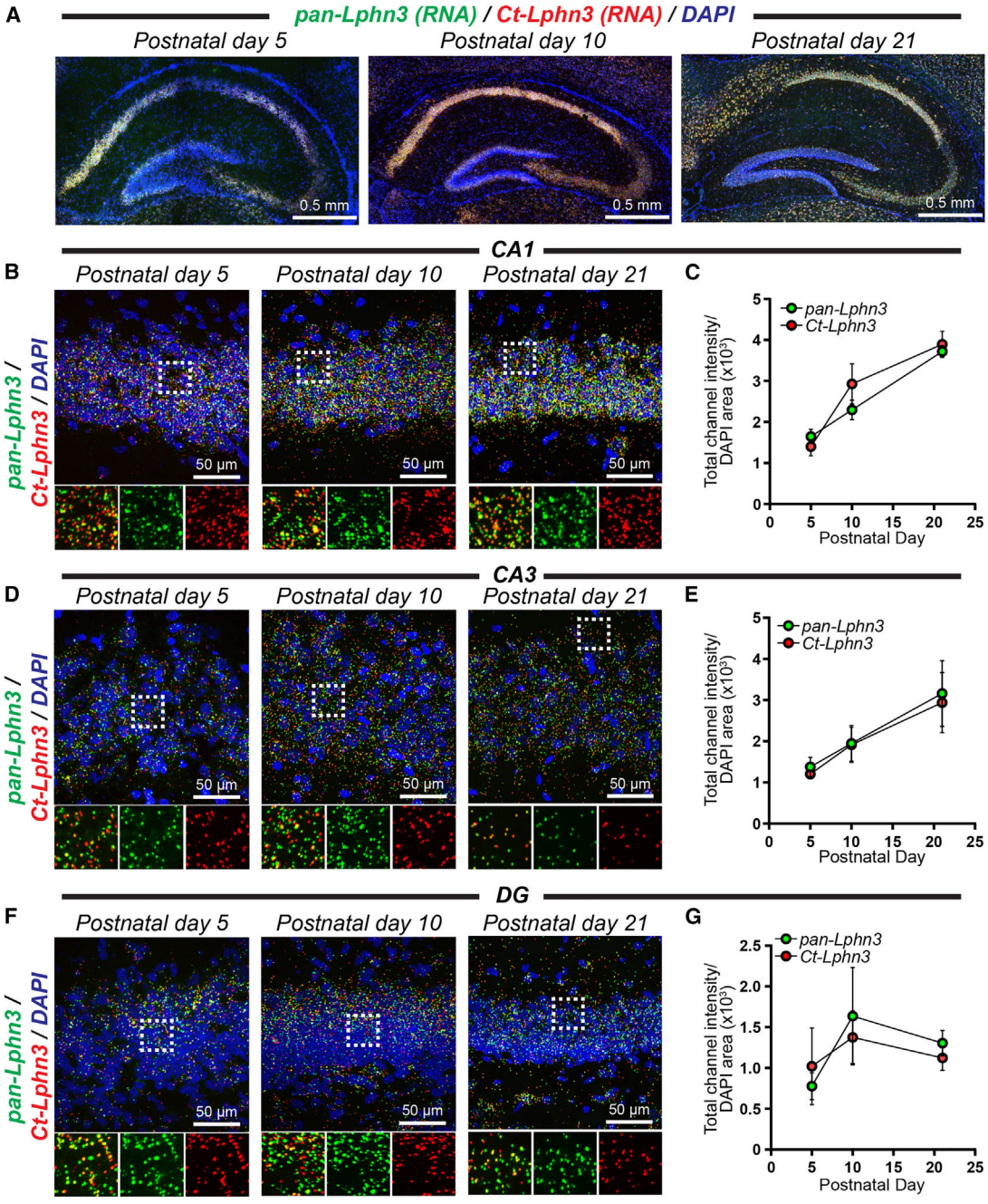

Figure 4. Total and splice-site-specific *Lphn3* spatial expression in the developing mouse hippocampus

(A) Representative images of the postnatal day 5, 10, and 21 mouse hippocampus labeled for RNA *in situ* probes for pan-Lphn3 transcripts together with a probe specific for the C-terminal tail sequence (Ct-Lphn3) that is present in Lphn3*tv*5 and Lphn3*tv*7 but not Lphn3*tv*9.

(B) Representative high-magnification 60× images of *in situ* hybridizations in the hippocampal CA1 region at postnatal day 5, 10, and 21. Top, representative merged channel

image; bottom, zoom in of white boxed area from the left with individual channels separated for pan-Lphn3 (green) and Ct-Lphn3 (red).

(C) Quantifications of CA1 RNA *in situ* results. The total channel intensity of green (pan-Lphn3) or red (Ct-Lphn3) signal was compared with the area occupied by DAPI for each respective image.

(D and E) Same as (B) and (C) except for the hippocampal CA3 region.

(F and G) Same as (B) and (C) except for the hippocampal dentate gyrus (DG). Numerical data are means ± SEM from 3–4 independent biological replicates.

See Figure S5 for additional *Lphn3* RNA *in situ* quantifications.

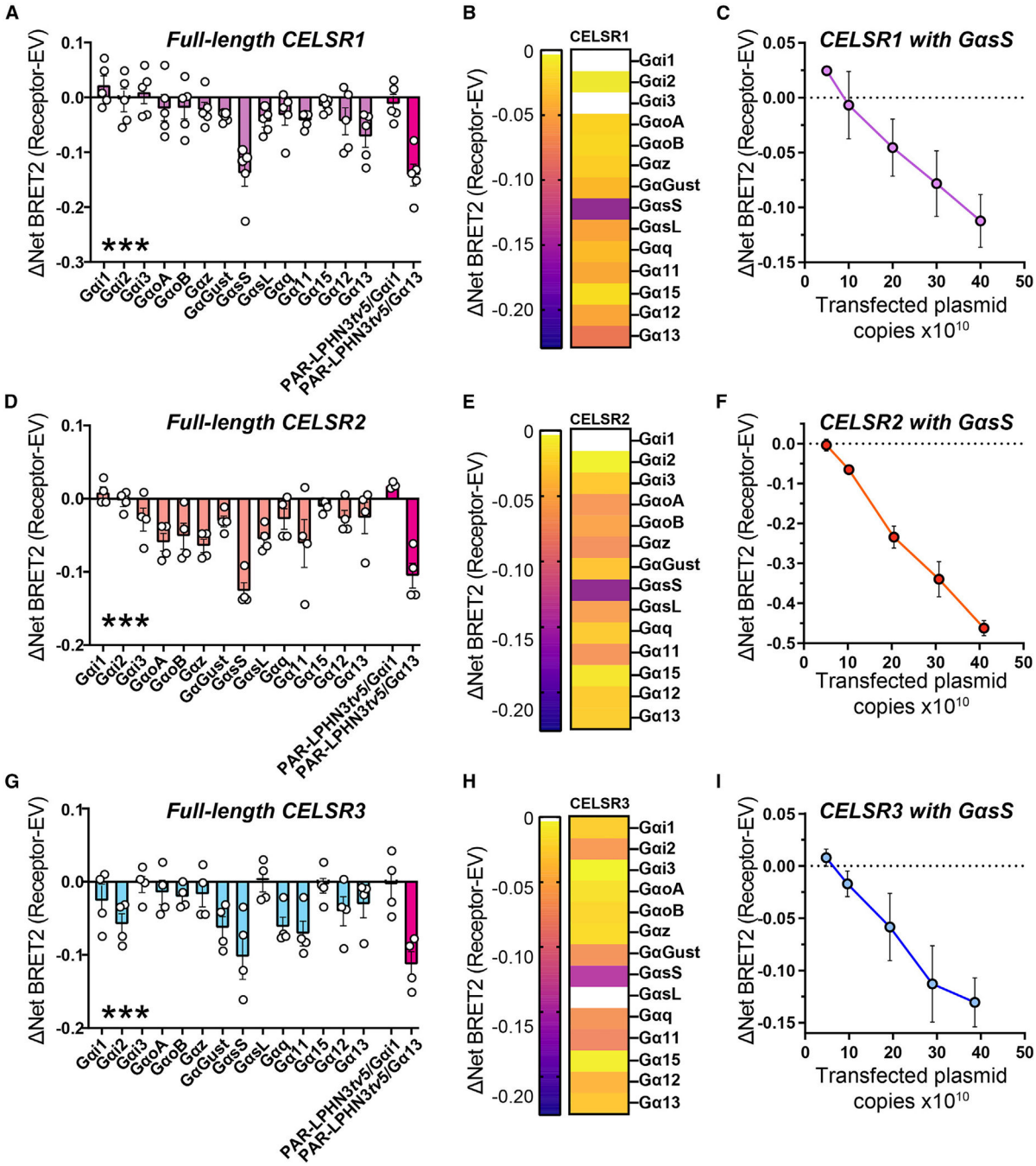

Figure 5. Full-length *Mm* CELSR1–3 are capable of GαsS coupling

(A) BRET2 assays with full-length *Mm* CELSR1 and the complete panel of TRUPATH sensors in GKO HEK293 cells to test G protein coupling. Basal activity of PAR-LPHN3*tv*5 with Gαi1 or Gα13 was used as the control in all experiments. Data are from 5 independent biological replicates, as depicted by open circles in graphs.

(B) Heatmap illustrating G protein coupling of full-length *Mm* CELSR1.

(C) Copy-dependent full-length *Mm* CELSR1 coupling to GαsS. GKO HEK293 cells were transfected with increasing amounts of full-length *Mm* CELSR1 and BRET2 measurements

conducted compared with cells transfected with the same total amount of empty vector. Data are from 3 independent biological replicates.

(D) Full-length *Mm* CELSR2 G protein coupling via BRET2. Experiments were conducted as in (A) except for CELSR2. Data are from 4 independent biological replicates.

(E) Heatmap illustrating G protein coupling of full-length *Mm* CELSR2.

(F) Copy-dependent full-length *Mm* CELSR2 coupling to GαsS. Experiments were performed as in (C), and data are from 3 independent biological replicates.

(G) Full-length *Mm* CELSR3 G protein coupling via BRET2. Experiments were conducted as in (A) except for CELSR3. Data are from 4 independent biological replicates.

(H) Heatmap illustrating G protein coupling of full-length *Mm* CELSR3.

(I) Copy-dependent full-length *Mm* CELSR3 coupling to GαsS. Experiments were performed as in (C), and data are from 3 independent biological replicates.

Numerical data are means ± SEM from 3–5 independent biological replicates (depicted as open circles in bar graphs), as indicated in the figure legends. Statistical significance was assessed by one-way ANOVA (***$p < 0.001$). Asterisks depict one-way ANOVA results. See Figure S6 for additional CELSR BRET2 data.

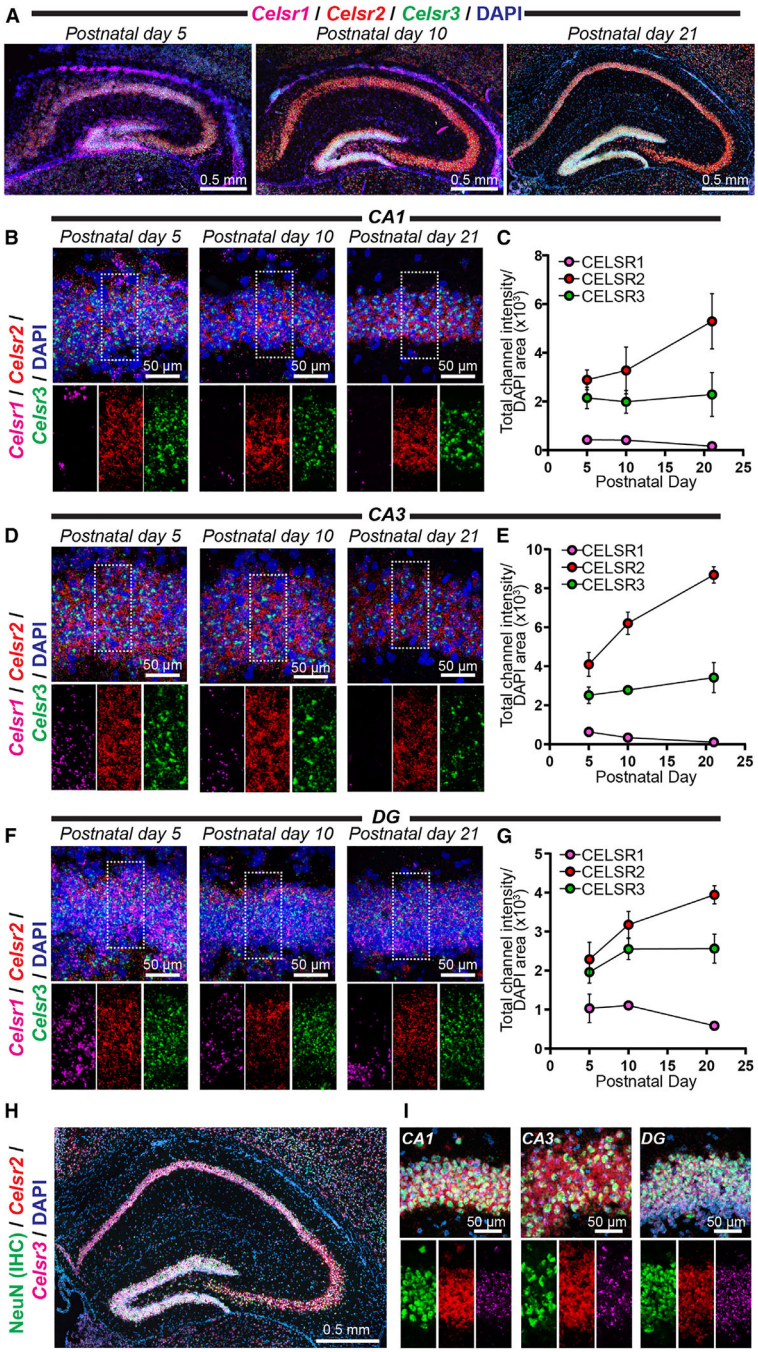

Figure 6. Partially overlapping *Celsr1–3* spatial expression during hippocampal circuit assembly

(A) Representative image of the postnatal day 5, 10, and 21 mouse hippocampus co-labeled with RNA *in situ* probes for *Celsr1–3* and DAPI.

(B) Representative high-magnification images of *in situ* hybridizations in the hippocampal CA1 region at postnatal days 5, 10, and 21. Top, representative merged channel image; bottom, zoom in highlighting the white boxed pyramidal cell layer area from the top with individual channels separated for *Celsr1* (magenta), *Celsr2* (red), and *Celsr3* (green).

(C) Quantifications of CA1 RNA *in situ* data. The total channel intensity of green (*Celsr3*), red (*Celsr2*), or far-red (*Celsr1*) signal was compared with the area occupied by DAPI for each respective image.
(D) Same as (B) except for the hippocampal CA3 region at postnatal days 5, 10, and 21.
(E) Quantifications of CA3-region RNA *in situ* data. Similar to (C) except for the hippocampal CA3 at postnatal days 5, 10, and 21.
(F) Same as (B) except for the hippocampal DG at postnatal days 5, 10, and 21.
(G) Quantifications of RNA *in situ* data from the DG. Similar to (C) except for the hippocampal DG at postnatal days 5, 10, and 21.
(H and I) Double immunohistochemistry (IHC) and RNA *in situ* hybridizations for the neuronal marker NeuN together with *Celsr2/3* RNA.
(H) Representative postnatal day 21 hippocampus co-labeled for NeuN (IHC; green), *Celsr2* (RNA *in situ*; red), *Celsr3* (RNA *in situ*; magenta), and DAPI.
(I) Representative high-magnification image of the postnatal day 21 hippocampal CA1, CA3, and DG from double IHC/RNA *in situ* experiments. Top, merged image depicting IHC for NeuN (green) together with RNA *in situ* hybridizations for *Celsr2* (red), *Celsr3* (magenta), and DAPI. Bottom, individual channel images for the center area of top highlighting *Celsr2/3* distribution. Numerical data are means ± SEM from 3–4 independent biological replicates.
See Figure S7 for additional *Celsr1–3* spatial expression data.

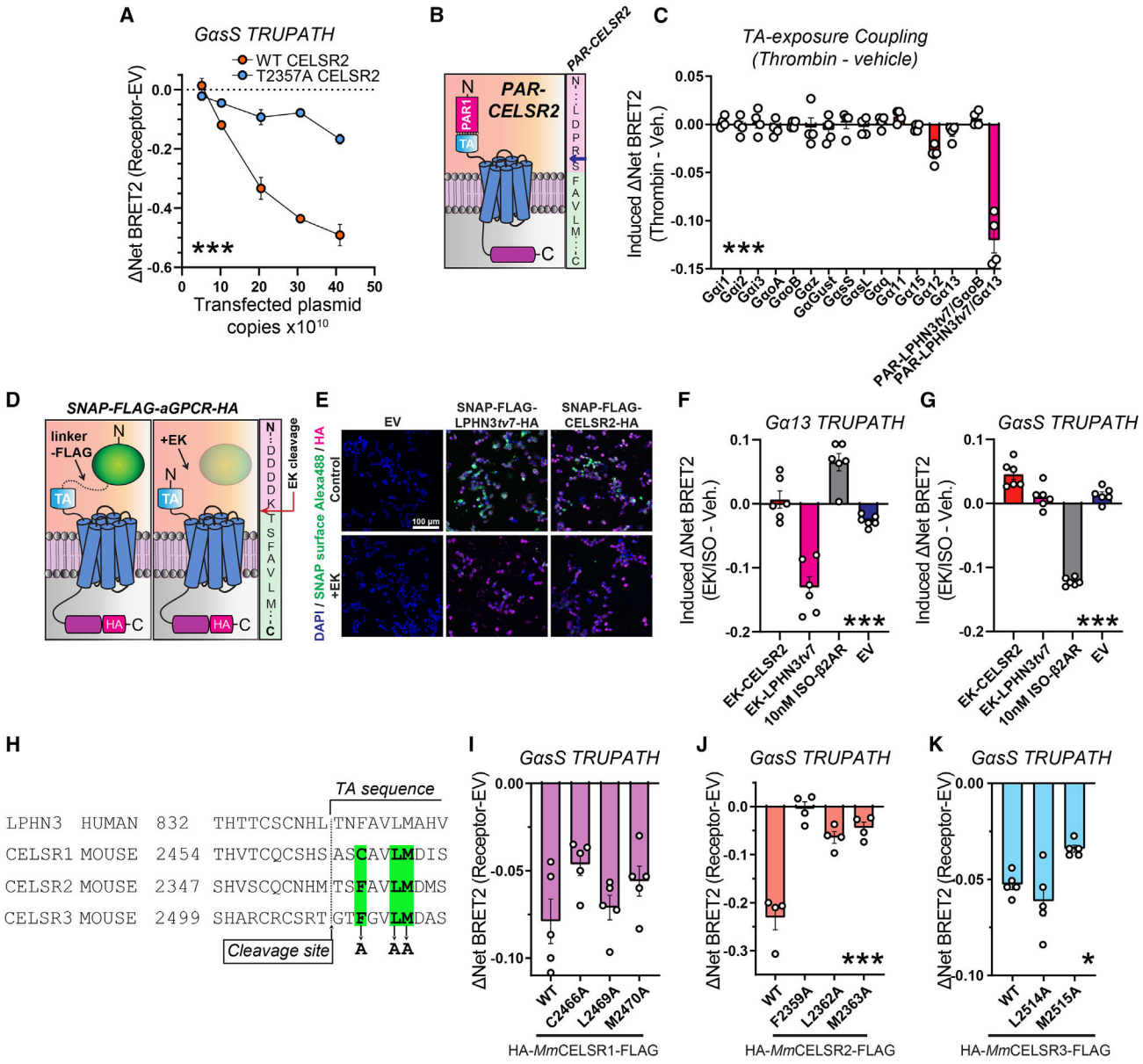

Figure 7. CELSRs engage distinct GαsS induction mechanisms

(A) Plasmid dose-dependent WT CELSR2 and T2357A CELSR2 GαsS coupling. Experiments were conducted as in Figure 5, except full-length T2357A CELSR2 was analyzed in parallel to full-length WT CELSR2.

(B) Left, schematic diagram for PAR-CELSR2. Right, illustration of PAR-CELSR2 cleavage site. Thrombin cleaves PAR (pink sequence) following arginine (blue arrow), exposing an N-terminal serine followed by the TA sequence (light green sequence).

(C) G protein coupling following acute TA exposure in PAR-CELSR2 using the complete panel of TRUPATH sensors. BRET2 measurements were conducted for four independent biological replicates. TA-induced coupling of PAR-LPHN3*tv7* with GαoB or with Gα13 were used as controls.

(D) Strategy for acute exposure of a native tethered agonist.[55,61] A SNAP tag-linker-FLAG sequence was fused immediately upstream the native tethered agonist sequence for LPHN3*tv7* or CELSR2. Enterokinase cleaves immediately following DDDK/ in FLAG, exposing the native TA peptide. The sequence on the right shows fusion region for CELSR2.
(E) Validation of surface expression and enterokinase-mediated cleavage of SNAP tags. HEK293T cells were transfected with indicated experimental or control (empty vector [EV]) plasmids in 24-well plates, treated with 32 U enterokinase vs. control, and labeled for cell-impermeable SNAP ligand conjugated to Alexa Fluor 488. Cells were subsequently fixed and immunolabeled for the C-terminal HA tag as an internal control.
(F) Gα13 coupling of indicated conditions. Transfected cells plated into 96-well plates were treated with 5.5 U/well enterokinase (EK) or vehicle for 15 min, and BRET2 was subsequently measured. β2-AR treated with 10 nM ISO and EV treated with EK were used as a controls. Data are from 6 independent biological replicates.
(G) GαsS coupling in indicated conditions. Same as (F) except the GαsS TRUPATH sensors were used.
(H) Multiple sequence alignment of the GAIN region of human LPHN3 and mouse CELSR1–3. Putative residues for TA-mediated agonism of CELSR1–3, which were systematically mutated to alanine to examine their contribution to GαsS induction, are highlighted in green.
(I) GαsS coupling in indicated full-length WT, C2466A, L2469A, and M2470A CELSR1 conditions. Data are from 5 independent biological replicates.
(J) Same as (I) except for full-length WT, F2359A, L2362A, and M2363A CELSR2. Data are from 4 independent biological replicates.
(K) Same as (I) except for full-length WT, L2514A, and M2515A CELSR3. Data are from 5 independent biological replicates.
Numerical data are means ± SEM from 3–6 independent biological replicates (depicted as open circles in bar graphs), as indicated in the figure legends. Statistical significance was assessed by two-way ANOVA (A) or one-way ANOVA (*$p < 0.05$; ***$p < 0.001$). Asterisks depict ANOVA results.
See Figure S8 for additional data regarding *Mm* CELSR2 G protein/β-arrestin coupling and Figure S9 for surface expression and autoproteolysis assays for conditions in (H)–(K).

KEY RESOURCES TABLE

REAGENT or RESOURCE	SOURCE	IDENTIFIER
Antibodies		
Anti-HA mouse	Covance/Biolegend	Covance Cat# MMS-101R; RRID:AB_291262
Anti-HA rabbit	Cell Signaling Technologies	Cell Signaling Technology Cat# 3724; RRID:AB_1549585
Anti-NeuN mouse	EMD Millipore	Millipore Cat# MAB377; RRID:AB_2298772
Goat anti-Mouse Alexa Fluor 488	ThermoFisher	Thermo Fisher Scientific Cat# A-11001; RRID:AB_2534069
Goat anti-Mouse Alexa Fluor 546	ThermoFisher	Thermo Fisher Scientific Cat# A-11003; RRID:AB_2534071
Goat anti-Mouse Alexa Fluor 647	ThermoFisher	Thermo Fisher Scientific Cat# A-21236; RRID:AB_2535805
Goat anti-rabbit Alexa Fluor 488	ThermoFisher	Thermo Fisher Scientific Cat# A-11034; RRID:AB_2576217
Goat anti-rabbit Alexa Fluor 546	ThermoFisher	Thermo Fisher Scientific Cat# A-11010; RRID:AB_2534077
Goat anti-rabbit Alexa Fluor 647	ThermoFisher	Thermo Fisher Scientific Cat# A-21245; RRID:AB_2535813
Goat anti-chicken Alexa Fluor 647	ThermoFisher	Thermo Fisher Scientific Cat# A-21449; RRID:AB_2535866
Goat anti-guinea pig Alexa Fluor 647	ThermoFisher	Thermo Fisher Scientific Cat# A-21450; RRID:AB_141882
HRP-conjugated goat anti-mouse secondary antibody	Biotium	Cat#20400–1mL
Phalloidin Alexa 647	ThermoFisher	A22287
Phalloidin-iFluor 405	Abcam	Ab178752
Anti-FLAG iFluor488 conjugate	Genscript	A01809
Anti-HA iFluor647 conjugate	Genscript	A01808
Opal 520	Akoya Biosciences	OP-001001
Opal 570	Akoya Biosciences	OP-001003
Opal 690	Akoya Biosciences	OP-001006
Bacterial and virus strains		
DH10β	ThermoFisher	18297010
Stellar cells	Takara	636763
Chemicals, peptides, and recombinant proteins		
Bovine Serum Albumin Fraction V	Roche	10735086001
Normal Goat Serum	Jackson Immunoresearch	005000121
Bovine Serum Albumin	Sigma	A3803
Coelenterazine-400a	NanoLight Technologies	340
DAPI	Roche	10236276001
DMEM	Gibco	11995065
Fetal Bovine Serum	Gibco	16000044

REAGENT or RESOURCE	SOURCE	IDENTIFIER
Hanks' balance Salt Solution	Gibco	14175095
HEPES	Sigma	H3375
Matrigel Membrane Matrix	ThermoFisher	CB-40234
Poly-D-lysine	Gibco	A38904–01
MEM Non-essential Amino Acid Solution	Sigma	M7145
Nano-Glo Live Cell Assay System	Promega	N2011
Opti-MEM	Gibco	31985070
Paraformaldehyde	Electron Microscopy Science	15714
Penicillin/Streptomycin	Corning	MT30002CI
Thrombin	Sigma	T4846
Isoproterenol	Sigma	I6504
TransIT-2020	Mirus	MIR5400
LipoD293	SignaGen Laboratories	SL100668
Versene	Gibco	15040066
Enterokinase, light chain	NEB	P8070S
SNAP-Surface Alexa Fluor 488	NEB	S9129S
Mouse *Adgrl3* RNAscope probe for Accession #NM_001359828.1 region 4660–5680 (Ct-Lphn3)	Advanced Cell Diagnostics	Mm-AdgrI3-O2-C2 #1046031-C2
Mouse *Adgrl3* RNAscope probe for Accession #NM_198702.2 region 2338–3312	Advanced Cell Diagnostics	Mm-Lphn3-C3 #317481-C3
Mouse *Celsrl* RNAscope probe for Accession #NM_009886.2 region 4742–5601	Advanced Cell Diagnostics	Mm-CeIsr1 #317931
Mouse *Celsr2* RNAscope probe for Accession #NM_001004177.2 region 3910–4817	Advanced Cell Diagnostics	Mm-CeIsr2-C2 #317941-C2
Mouse *Celsr3* RNAscope probe for Accession #NM_080437.2 region 7034–7885	Advanced Cell Diagnostics	Mm-CeIsr3-C3 #319241-C3
RNAscope Mutliplex Fluorescent manual assay	Advanced Cell Diagnostics	323100
RNA-protein Co-detection ancillary kit	Advanced Cell Diagnostics	323180
To-Pro	ThermoFisher	T3605
0.45 μm pore nitrocellulose membrane	Bio-Rad	1620251
Kaleidoscope protein standard	Bio-Rad	1610375
PageRuler protein standard	Thermo	26619
Prolong Gold Antifade Reagent	Invitrogen	P36930
Experimental models: Cell lines		
HEK293T	ATCC	CRL-11268
GKO HEK293	Kind gift from Asuka Inoue, Tokyo University	Alvarez-Curto et al.,[58] J Biol Chem. Grundmann et al.,[59] Nat Commun.
Arr-2/3 KO HEK293	Kind gift from V.V. Gurevich, Vanderbilt University	Alvarez-Curto et al.,[58] J Biol Chem. Grundmann et al.,[59] Nat Commun.
Experimental models: Organisms/strains		
C57/BL6J	Jackson Laboratories	000664
Oligonucleotides		

REAGENT or RESOURCE	SOURCE	IDENTIFIER
Various cloning primers	IDT	N/A
Recombinant DNA		
pEB PAR-Lphn3*tv*5	This study	N/A
pEB PAR-Lphn3*tv*7	This study	N/A
pEB PAR-Lphn3*tv*9	This study	N/A
pEB HA-Celsr1-FLAG	This study	N/A
pEB HA-Celsr1 A2464T-FLAG	This study	N/A
pEB HA-Celsr2-FLAG	This study	N/A
pEB HA-Celsr2 T2357A-FLAG	This study	N/A
pEB HA-Celsr2 T2357G-FLAG	This study	N/A
pEB HA-Celsr3-FLAG	This study	N/A
pEB PAR-Celsr2	This study	N/A
pEB SNAP-FLAG-Lphn3*tv*7-HA	This study	N/A
pEB SNAP-FLAG-Celsr2-HA	This study	N/A
pEB HA-Celsr1 C2466A-FLAG	This study	N/A
pEB HA-Celsr1 L2469A-FLAG	This study	N/A
pEB HA-Celsr1 M2470A-FLAG	This study	N/A
pEB HA-Celsr2 F2359A-FLAG	This study	N/A
pEB HA-Celsr2 L2362A-FLAG	This study	N/A
pEB HA-Celsr2 M2363A-FLAG	This study	N/A
pEB HA-Celsr3 F2511A-FLAG	This study	N/A
pEB HA-Celsr3 L2514A-FLAG	This study	N/A
pEB HA-Celsr3 M2515A-FLAG	This study	N/A
TRUPATH kit	Addgene	1000000163
pcDNA3.1 FLAG-β_2-Adrenergic receptor	Addgene	14697
pCMV-hsLphn3	Lu etal., 2015, Structure[64]	N/A
Membrane-anchored LgBiT (AG10-CAAX)	Spillman et al., 2020[62]	N/A
pEB *Mm*-Arr2-SmBiT	This study	N/A
pEB *Mm*-Arr3-SmBit	This study	N/A
pEB *Mm* GRK2	This study	N/A
Software		
SnapGene	GSL Biotech	N/A
NIS-Elements AR	Nikon	N/A
ImageJ	National Institutes of Health	N/A
Adobe Photoshop	Adobe	N/A
Adobe Illustrator	Adobe	N/A
Graphpad Prism 8.0, 9.0	Graphpad	N/A